https://doi.org/10.5194/essd-2026-689
Preprint. Discussion started: 2 November 2026
© Author(s) 2026. CC BY 4.0 License.



Open Access Earth System Science Data Discussions

NH-SDN: A Deep Learning-Derived Daily 0.25° Snow Density Dataset for the Northern Hemisphere from 1982–2025

Li Zhong[1], Xueliang Zhang[1,*], Yuwen Lin[1], Dongyang Du[1], Yixi Bi[1], Liyang Sun[1], Yantao Liu[1], Jiale Geng[1], Sijie Zhao[1], Pengfeng Xiao[1,2]

[1]Jiangsu Provincial Key Laboratory for Advanced Remote Sensing and Geographic Information Technology, Key Laboratory for Land Satellite Remote Sensing Applications of Ministry of Natural Resources, School of Geography and Ocean Science, Nanjing University, Nanjing, Jiangsu 210023, China
[2]Jiangsu Center for Collaborative Innovation in Geographical Information Resource Development and Application, Nanjing, Jiangsu 210023, China

Correspondence to: Xueliang Zhang (zxl@nju.edu.cn)

Abstract. Snow density is a key parameter in the physical properties of the snowpack. Accurately mapping snow density is essential for water resources, avalanche hazards, and snowpack thermal processes. However, large-scale snow density datasets that provide reliable accuracy, spatial and temporal continuity, and comprehensive coverage across the Northern Hemisphere remain unavailable. To bridge this gap, we develop SDN-Net, a spatiotemporal framework integrating vision Transformers and convolutional neural networks, to capture global dependencies and local heterogeneity for snow density estimation. The framework incorporates multisource environmental variables and leverages adaptive feature refinement mechanisms to better characterize temporal variations in snow density. Using this framework, we develop NH-SDN, a daily snow density dataset for the Northern Hemisphere at a spatial resolution of 0.25° from 1982–2025. Compared with reanalysis datasets covering the Northern Hemisphere, NH-SDN shows higher accuracy across all months, particularly from March to May, where RMSE decreases from 0.130 g cm^{-3} in reanalysis products to 0.053 g cm^{-3} in NH-SDN. It also performs well across different snow classes and elevations, with particularly notable improvements in mountainous regions above 2-km elevation, where systematic bias in reanalysis data is effectively reduced, and RMSE decreases from 0.100 to 0.042 g cm^{-3}. In addition, NH-SDN reduces the excessive smoothing of increase-stage variability and the overestimation of melt-stage trends in reanalysis products, allowing improved representation of interannual snow density variations. It also provides a continuous snow density dataset that closely agrees with in-situ measurements. The dataset provides a reliable basis for large-scale snowpack characterization and may support applications in snow water equivalent estimation, hydrological and cryospheric modeling, and snow thermal process studies. The dataset is available at https://doi.org/10.5281/zenodo.23768969 (Zhang et al., 2026).

https://doi.org/10.5194/essd-2026-689
Preprint. Discussion started: 2 November 2026
© Author(s) 2026. CC BY 4.0 License.



Open Access Earth System Science Data Discussions

1 Introduction

Snow covers vast regions of the Northern Hemisphere and plays a fundamental role in the global water and energy cycles (Brucker et al., 2011; Huning and AghaKouchak, 2020; Pulliainen et al., 2020). Snow density, as a key parameter characterizing snowpack physical properties, exhibits substantial spatiotemporal variability. Accurate snow density mapping is essential for improving snow water equivalent (SWE) estimation and runoff prediction, as uncertainties in snow density can propagate into substantial errors in water resource assessments (Barnett et al., 2005; Venäläinen et al., 2023; Yang et al., 2020). It also plays an important role in avalanche hazard modeling, as snow density is a key factor determining snowpack stability (Meloche et al., 2024). Moreover, it is critical for snowpack thermal insulation, as its spatiotemporal variability regulates snow thermal conductivity and plays an important role in determining ground thermal regimes and permafrost extent (Cao et al., 2022; Gouttevin et al., 2012; Mavrovic et al., 2023).

Existing snow density datasets have been developed through various approaches. In-situ observation methods obtain snow density datasets through direct field measurements, including manual snow surveys, snow pillows, and other automated monitoring systems. Extensive observation networks have been established in many snow-covered regions, including snow survey programs and meteorological monitoring systems, providing valuable information for investigating the spatial and temporal variability of snow density (Serreze et al., 1999; Cowherd et al., 2024; Meromy et al., 2013; Singh et al., 2024; Meehan et al., 2024). However, in-situ observations are spatially sparse, unevenly distributed, and subject to inconsistent measurement standards (Che et al., 2025; Hao et al., 2021; Zhao et al., 2023).

Process-based modeling approaches generate reanalysis snow density datasets by integrating land surface schemes and assimilation systems. These datasets, including ERA5-Land, GLDAS, and JRA-3Q, provide spatially and temporally continuous snow density estimates across most snow-covered regions of the Northern Hemisphere (Muñoz-Sabater et al., 2021; Rodell et al., 2004; Kosaka et al., 2024). They simulate snow density by parameterizing snow processes using formulations derived from process-based models such as CROCUS (Lee and Wang, 2009) and have become important data sources for large-scale investigations of snowpack dynamics and hydrological processes. However, reanalysis datasets rely on model parameterizations and meteorological forcing (Dutra et al., 2010), which can introduce uncertainties into snow density estimates. They often exhibit systematic underestimation relative to in-situ observations and have limited ability to capture interannual variability (Li et al., 2026).

Remote sensing approaches generate snow density datasets by exploiting the sensitivity of microwave signals to snowpack properties. Active microwave approaches, such as those demonstrated by Dozier and Shi (2000) with L-band dual-polarization data and by Li et al. (2022) with C-band SAR, estimate density by isolating volume and surface scattering contributions. Passive microwave approaches, including the work of Champollion et al. (2019) using the 37 GHz polarization ratio and Gao et al. (2023) using SMOS L-band multi-angle observations, rely on brightness temperature signatures. However, a cross-cutting limitation unites these two pathways: irrespective of the technique, the snow density

https://doi.org/10.5194/essd-2026-689
Preprint. Discussion started: 2 November 2026
© Author(s) 2026. CC BY 4.0 License.

Open Access Earth System Science Data Discussions

signal is notoriously weak compared to the dominant influences of grain size and liquid water content (Gao et al., 2022; Kneifel et al., 2010). Other snowpack parameters easily mask the density signal, and the coupled effects of multiple variables are difficult to isolate from microwave observations (Cao and Barros, 2023; Lievens et al., 2019). Moreover, most retrieval algorithms are built on site-specific empirical or semiempirical relations, whose applicability is limited to particular snow regimes and climatic conditions, preventing large-scale or global extension.

Machine learning approaches have increasingly been adopted to model the relation between snow density and its environmental controls (Sturm et al., 2010). Early studies mainly estimated snow density using multiple linear regression models driven by variables such as snow depth (SD) and air temperature (Bormann et al., 2013; Jonas et al., 2009; Valt et al., 2018). Bayesian models and artificial neural networks are capable of capturing complex nonlinear relations between snow density and its influencing factors, and have been applied in regions such as Norway and the western United States (Broxton et al., 2019; Bruland et al., 2015). Methods such as the geographically and temporally weighted neural network (GTWNN) and the spatiotemporal random forest (STRF) explicitly integrate spatiotemporal information along with meteorological, vegetation, terrain, and snow-related covariates and have been applied to regional snow density mapping in China (Sun et al., 2024a; Wang et al., 2023). However, the complex spatiotemporal evolution of snow density across different climatic and environmental conditions of the Northern Hemisphere poses substantial challenges to generating large-scale datasets. Snow density is influenced by meteorological conditions, terrain characteristics, vegetation cover, and snowpack evolution processes. During snowfall, snow density is influenced by moisture availability and air temperature, whereas after deposition, the snowpack undergoes transformations, including compaction, temperature-gradient metamorphism, melt–refreeze cycles, and wind-induced redistribution (Bormann et al., 2013; Roebber et al., 2003). Therefore, snow density exhibits spatial heterogeneity and seasonal variability among different snow classes and climatic regions of the Northern Hemisphere (Sturm and Liston, 2021; Zhao et al., 2023). Despite the potential of machine learning, existing models treat snow density estimation as a static relation, overlooking the varying controls across snow evolution stages. Moreover, they typically perform inference at isolated spatiotemporal points, ignoring contextual influences from neighboring times and locations. This restricts their spatial continuity and generalization, confining their applicability to localized regions. Consequently, effective and scalable methodologies for generating spatially continuous, high-quality Northern Hemisphere snow density products remain critically lacking.

Collectively, existing approaches do not yet provide snow density estimates that are accurate, spatially continuous, temporally resolved, and reliable across the diverse climatic and snow regimes of the Northern Hemisphere. This limitation constrains the reliable assessment of long-term changes in snow density. Existing products may reproduce broad spatial patterns and seasonal variability, yet often misrepresent observed interannual trends by underestimating early-winter changes or shifting them to later winter (Li et al., 2026). It also affects hydrological and thermal applications. For example, in SWE estimation, even a simple spatial interpolation of snow density can improve accuracy by up to 16% compared with the use of a fixed density value (Venäläinen et al., 2023; Yang et al., 2020). Within process-based models and data assimilation

https://doi.org/10.5194/essd-2026-689
Preprint. Discussion started: 2 November 2026
© Author(s) 2026. CC BY 4.0 License.



systems, biases in snow density may offset or amplify SWE biases, resulting in region- and dataset-dependent errors in simulated SD (Li et al., 2026). In land-surface and permafrost modeling, snow density errors alter snow thermal conductivity and insulation, leading to biases in ground heat flux, soil temperature, and simulated permafrost extent (Cao et al., 2020, 2022). These limitations create an urgent need for a high-quality snow density dataset that provides accurate, spatially continuous, and temporally resolved estimates across diverse snow regimes, enabling reliable assessment of long-term variability and reducing uncertainties in hydrological and thermal applications.

In response to these limitations, this study presents a deep learning-based snow density estimation model SDN-Net, and the NH-SDN dataset, a daily 0.25° snow density dataset for the Northern Hemisphere spanning 1982–2025. SDN-Net is trained using quality-controlled in-situ snow density observations from North America and Eurasia and integrates multisource environmental variables associated with snow conditions, meteorological forcing, vegetation dynamics, topography, geographic location, and temporal evolution. Compared with conventional machine learning approaches, the deep learning framework captures nonlinear relations between snow density observations and environmental controls, with input features optimized across different regions and snow density evolution stages to better represent heterogeneous snowpack processes. By incorporating snow density evolution stages and spatiotemporal contextual information, SDN-Net dynamically captures the changing controls on snow density rather than relying on static local relations. The Vision Transformer (ViT)-Convolutional Neural Network (CNN) architecture further enables the model to characterize both large-scale spatial dependencies and local heterogeneity, improving spatial continuity and regional-scale generalization. Supported by the advantages of SDN-Net, the NH-SDN dataset provides spatially continuous and temporally consistent snow density estimates across the Northern Hemisphere, overcoming the limitations of sparse observations and existing model-based products. Comprehensive evaluations against independent in-situ measurements and multiple reanalysis datasets across different snow classes, regions, elevations, and temporal scales demonstrate improved accuracy and enhanced capability in representing seasonal variations, interannual variability, and long-term trends. The dataset provides a reliable basis for large-scale snowpack characterization, with applications including snow water equivalent estimation, hydrological modeling, avalanche assessment, snow thermal process studies, and climate change research.

2 Data

2.1 In-situ data

An extensive in-situ snow density dataset is compiled by integrating observations from multiple networks and historical archives, including NorSWE, CanSWE, SNOTEL, RIHMI-WDC, historical Union of Soviet Socialist Republics (USSR) snow surveys, European meteorological stations, and the China Meteorological Administration (CMA), covering more than 10,000 stations from 1979 to 2021 and yielding approximately 3 million records (Table 1). The Northern Hemisphere historical in-situ snow water equivalent dataset (NorSWE; Fontrodona-Bach et al., 2023; Mortimer and Vionnet, 2025)

https://doi.org/10.5194/essd-2026-689
Preprint. Discussion started: 2 November 2026
© Author(s) 2026. CC BY 4.0 License.



provides an important basis for this compilation by integrating multi-source snow observations from 11 agencies across the Northern Hemisphere. NorSWE includes manual snow surveys, automated measurements from snow pillows, snow scales, and passive gamma radiation sensors, airborne gamma SWE observations, and long-term snow course measurements from North America, Eurasia, and Europe. Snow density observations are derived from paired snow depth and snow water equivalent measurements. The data sources included in NorSWE are further examined to obtain available SD–SWE observations for snow density estimation. These sources include the Canadian CanSWE dataset, which combines multi-point snow course surveys and automated snow pillow observations (Brown et al., 2019; Vionnet et al., 2021), the SNOTEL network, which provides continuous daily measurements using snow pillows and ultrasonic snow depth sensors across the western United States (Dawson et al., 2016; Fassnacht et al., 2003), and Eurasian observations from RIHMI-WDC and historical USSR snow surveys, which are based on large-scale snow transect investigations with regular spatial sampling intervals and meteorological station measurements (Brun et al., 2013; Bulygina et al., 2011). These complementary records are incorporated when they provide additional observations beyond those available in the NorSWE compilation, and potential overlaps among all datasets are identified and removed during data integration. Furthermore, independent observations from meteorological stations in Europe and China are added to further extend the spatial and temporal coverage. These station records, mainly from France Meteorological Administration (FMA) and the China Meteorological Administration (CMA), are not included in NorSWE and are therefore integrated as separate data sources. Despite the extensive coverage, substantial differences remain among these datasets in terms of observation frequency, sampling density, and measurement principles due to variations in observation protocols and sensor types. Manual snow surveys generally provide stronger spatial representativeness through multi-point sampling, whereas automated systems offer higher temporal continuity and measurement stability. Such methodological differences introduce unavoidable heterogeneity among the merged observations, which cannot be fully eliminated during data integration. Therefore, a unified quality-control procedure is applied to minimize erroneous records and improve the reliability of the final dataset.

Quality control is performed following established procedures (Mortimer and Vionnet, 2025). Observations with physically unrealistic values are removed, including SD exceeding 3 m (or 8 m for mountain sites), snow water equivalent exceeding 3000 mm (or 8000 mm for mountain sites), and snow density outside the range of 0.025–0.7 g cm^{-3}. For automated stations with sufficient paired measurements, spurious SD–SWE combinations are identified using the robust-sample Mahalanobis distance (Leys et al., 2018), which detects multivariate outliers based on their deviation from the central distribution while accounting for covariance among variables. This procedure helps remove physically inconsistent SD–SWE relations that cannot be detected through independent range filtering alone. Stations with fewer than 20 valid observations are excluded to retain a more robust dataset.

The spatial distribution and temporal coverage of Northern Hemisphere snow density observations after quality control are summarized in Fig. 1. In terms of spatial heterogeneity, each station is assigned to a snow class based on the global seasonal snow classification (Sturm and Liston, 2021). Snow density exhibits distinct variations across elevation gradients and snow classes (Fig. 1a). Higher densities are generally observed in maritime and ephemeral classes, whereas boreal forest and

https://doi.org/10.5194/essd-2026-689
Preprint. Discussion started: 2 November 2026
© Author(s) 2026. CC BY 4.0 License.



tundra classes show relatively lower values. These variations reflect the complex snow conditions across the Northern Hemisphere and highlight the need for models with strong generalization capability across diverse snow regimes. A weighted Two-Phase Regression (TPR) method is applied to detect changepoints in multi-year mean snow density curves and characterize regional differences in seasonal snow density evolution (Reeves et al., 2007). The results reveal distinct snow density evolution patterns between Eurasia and North America (Fig. 1b). Eurasia is characterized by three stages, including increase, stable, and decrease stages, whereas North America exhibits an additional consolidation stage between the increase and decrease stages. In Eurasia, snow density increases gradually during the increase stage and remains relatively stable during mid-winter. In contrast, North America experiences a faster density increase during the consolidation stage, likely associated with stronger continental cold-air influences and enhanced snowpack compaction. In both regions, late-spring warming and snowmelt trigger snowpack destabilization and a rapid decline in snow density. These contrasting seasonal evolution patterns between Eurasia and North America motivate separate model training for the two regions to better capture their distinct snowpack processes. Fig. 1c shows interannual variability in seasonal snow density evolution and uneven observational coverage. These patterns support combining seasonal descriptors with time-varying environmental predictors and highlight the need to assess model generalization through independent temporal testing.

Table 1. Summary of in-situ observations from multiple sources.

Country	Data source / Agency	Measurement methods	Data access	Period	No. of stations	No. of samples
Canada	CanSWE v6 (Environment and Climate Change Canada)	Snow course, snow pillows, passive gamma radiation sensors, acoustic SD sensor	CanSWE website	1979–2021	2574	344,485
USA	USDA NRCS Snow Survey & SNOTEL	Snow course, snow pillows, snow scale, acoustic SD sensor	NRCS website, soilDB	1979–2021	5533	2,137,457
	Maine Geological Survey	Snow course	Maine Open Data	1979–2021	360	19,015
	Northeast Regional Climate Center (NRCC)	Snow course	NRCC website	1979–2021	797	17,287
	New Hampshire DES Dams	Snow course	NH DES website	1979–2020	25	2,373
Finland	Finnish Environmental Institute (SYKE)	Snow course	SYKE API	1979–1992	10	1,558
Russia	RIHMI-WDC	Snow course	RIHMI-WDC website	1979–2020	633	302,741
	FSU Snow Survey (USSR Hydromet)	Fixed snow stakes, transect surveys, manual SWE measurement	NSIDC	1979–1996	62	2,179
Norway	NVE	Snow pillows/snow scale / acoustic SD sensor	NorSWE / NorEEN	1979–2021	18	27,804
Switzerland	WSL / SLF	Manual SWE and SD (single point)	Envidat GCOS SWE	1979–2021	15	3,671
France	FMA & Col de Porte (CENACLAM)	Ultrasonic depth sensor, laser rangefinder, manual snow pit	PANGAEA / NSIDC	1996–2021	137	47,108
China	CMA & National Climate Center	Snow ruler, gravimetric sampling, automatic SD sensor, microwave retrieval	CMA	2013–2020	159	11,672

https://doi.org/10.5194/essd-2026-689
Preprint. Discussion started: 2 November 2026
© Author(s) 2026. CC BY 4.0 License.

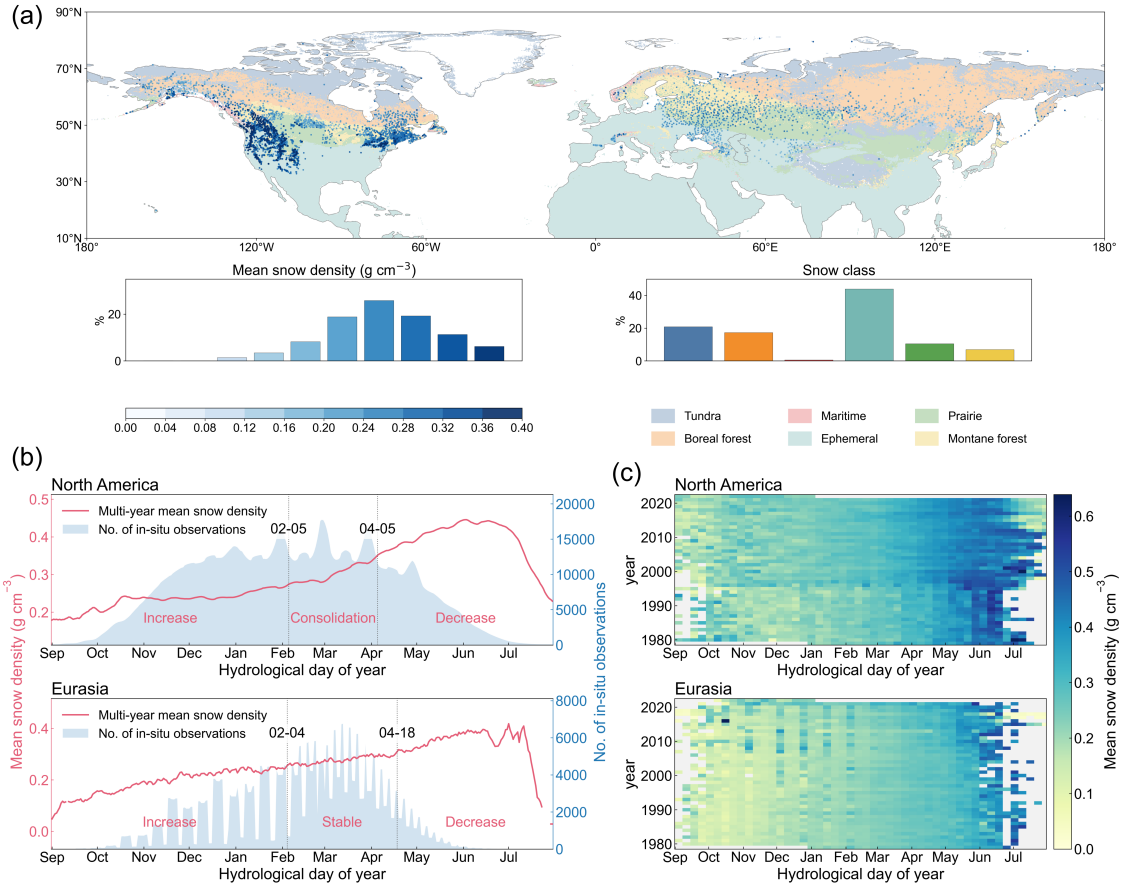


Figure 1. Spatial distribution and temporal variability of quality-controlled in-situ snow density observations across the Northern Hemisphere. (a) Station-level multi-year mean snow density overlaid on snow classes. Histograms summarize the distribution of station-mean density and the proportions of snow-class grid cells. (b) Mean hydrological-year cycles of snow density (rose-red curves) and observation counts (blue shading) in North America and Eurasia. Vertical dotted lines mark transitions between snow density development stages identified using TPR: increase, consolidation, and decrease in North America; increase, stable, and decrease in Eurasia. (c) Year-by-year seasonal variations in mean snow density across the observational record; blank cells indicate missing observations.

2.2 Remote sensing and reanalysis data

Multisource reanalysis, remote sensing, and ancillary geographic data are integrated to characterize the physical controls and spatiotemporal heterogeneity of snow density. The input data are grouped into three categories: dynamic environmental data, static geographic variables, and temporal descriptors.

Dynamic environmental data include snow-related data and meteorological data. Snow-related data, including snow albedo, snow cover fraction, snow density, snow depth, snowfall, snow pressure, snow surface temperature, and so on, are mainly

https://doi.org/10.5194/essd-2026-689
Preprint. Discussion started: 2 November 2026
© Author(s) 2026. CC BY 4.0 License.



obtained from ERA5-Land (land component of the fifth generation of European Reanalysis) (Muñoz-Sabater et al., 2021). ERA5-Land snow density is used as prior knowledge to provide baseline snow-density information for model estimation, which is derived from land surface schemes in which snow density is parameterized using formulations from process-based snow models, relying on model parameterization and meteorological forcing (Dutra et al., 2010); Snow depth, snowfall, snow pressure, and snow-layer temperature are included to represent snow accumulation, compaction, metamorphism, and melt processes (Bormann et al., 2013; Mizukami and Perica, 2008), as these factors collectively determine the post-depositional evolution of snow density (Roebber et al., 2003). Meteorological data, including air temperature, precipitation, air pressure, wind speed, surface temperature, and soil temperature, are also extracted from ERA5-Land, as they regulate fresh-snow density, surface energy exchange, vapor gradients, freeze–thaw cycles, and post-depositional snow evolution (Rasmus, 2013). Specifically, air temperature and pressure govern snow crystal growth and settling (Meløysund et al., 2007), while wind speed affects snowpack compaction and redistribution (Kozlov, 2001). Vegetation data, represented by high-vegetation and low-vegetation leaf area indices, are used to account for canopy effects on snow interception, radiation transfer, and snowpack densification by modifying snow depth and sub-canopy energy fluxes (Bonner et al., 2022; Clark et al., 2011; Winstral and Marks, 2014).

Static geographic variables include geographic location, topography, and snow-zone information. Longitude and latitude are introduced to explicitly represent large-scale spatial gradients and regional differences in snow-density distribution, because snow density varies substantially with climatic background, continentality, and geographic position (Clark et al., 2011; Zhong et al., 2021).

Static topographic variables, including elevation, slope, and aspect, are derived from the Global Multi-resolution Terrain Elevation Data 2010 (GMTED2010) (Carabajal et al., 2011), which is primarily based on Shuttle Radar Topography Mission (SRTM) DEM data. These variables characterize terrain-induced differences in radiation receipt, temperature, snow redistribution, and melt conditions (Wetlaufer et al., 2016). The global seasonal snow classification is used to distinguish different snow classes (Sturm and Liston, 2021), including tundra, boreal forest, prairie, montane forest, maritime, and ephemeral snow.

Temporal descriptors are designed at the hydrological-year scale because snow density exhibits a clear seasonal evolution pattern, generally increasing as snow accumulates and the snowpack compacts, and decreasing during snowmelt periods (Dai et al., 2012). The hydrological year is therefore represented by the temporal distance to September 1st. To further characterize seasonal radiative forcing, the latitude of direct sunlight and its changing speed are additionally introduced as auxiliary temporal variables.

The solar declination l and its rate of change v are given by Eqs. (1) and (2), respectively:

$$l=23.43\times \sin\left(2\times\pi\times\frac{d-81}{366}\right), \quad (1)$$

$$v=\frac{dl}{dt}=\frac{23.43\times2\times\pi}{366}\times\cos\left(2\times\pi\times\frac{d-81}{366}\right), \quad (2)$$

https://doi.org/10.5194/essd-2026-689
Preprint. Discussion started: 2 November 2026
© Author(s) 2026. CC BY 4.0 License.



where d is the Julian day. Equation (1) represents the latitude of direct sunlight, also known as solar declination, while Eq. (2) gives its instantaneous rate of change with respect to time.

The SHAP (Shapley Additive exPlanations) analysis is applied to all candidate input features listed in Table 2 to investigate the dominant controls on snow density at different evolution stages. Based on Shapley values, the contribution of each input feature to model predictions is quantified (Lundberg and Lee, 2017). We conduct SHAP analysis separately for North America and Eurasia at each stage to identify the most influential variables and to reveal regional and evolutionary differences.

The influencing factors of snow density exhibit pronounced stage-dependent and region-dependent differences (Fig. 2). In both North America and Eurasia, the prior snow-density distribution consistently exhibits the highest contribution throughout all snow-evolution stages, indicating that reanalysis-derived snow density from physical models provides strong prior information for snow density estimation. In North America, air temperature plays a dominant role during the increase stage, when fresh snow density is strongly controlled by atmospheric thermal processes. During the consolidation stage, underlying surface conditions become more influential due to rapid snow compaction. In the decrease stage, topographic factors, such as aspect-related wind redistribution, together with meteorological forcing, exert stronger control on snow density. In Eurasia, latitudinal and longitudinal gradients remain consistently important, with meteorological and snow-related factors dominating the increase and stable stages, while topography exerts a stronger influence during the decrease stage. These distinct regional and stage-dependent controls indicate that North America and Eurasia require different feature combinations and separate model training to better capture their unique snow-density evolution processes. Since the channel attention mechanism in SDN-Net can dynamically adjust the contributions of input variables across snow density evolution stages, a single model is trained for each region using a fixed input set. Specifically, for each region, the 14 variables with the highest mean absolute SHAP values were selected at each snow density evolution stage (Fig. 2). The union of environmental variables among these stage-specific selections yields 12 environmental inputs for North America and 13 for Eurasia. Both regional models additionally retain longitude, latitude, elevation, slope, aspect, and snow class, together with the temporal descriptors. These auxiliary inputs provide geographic constraints and seasonal context through the encoder branches, temporal embeddings, and Static-Time FiLM module (Section 3.2.1). The complete final input lists for North America and Eurasia are provided in Tables B1 and B2, respectively.

We choose two widely used reanalysis products, GLDAS-Noah (v2.0) and ERA5-Land, to evaluate the performance of the proposed dataset. Compared with other reanalysis datasets, GLDAS-Noah and ERA5-Land show relatively better performance over the Northern Hemisphere (Li et al., 2026). Therefore, we use these two products as benchmarks to evaluate the effectiveness of NH-SDN. GLDAS-Noah provides SD and SWE simulated by its land surface model, from which snow density is calculated as the ratio of SWE to SD. The original 3-hourly outputs are aggregated to daily values, with accumulated variables (e.g., snowfall) summed over each day and instantaneous variables (e.g., SD) averaged to obtain daily means (Rodell et al., 2004). ERA5-Land is also used as a benchmark, although its physically based snow density estimates are included as input features in NH-SDN. Comparing NH-SDN with ERA5-Land further quantifies the extent to

https://doi.org/10.5194/essd-2026-689
Preprint. Discussion started: 2 November 2026
© Author(s) 2026. CC BY 4.0 License.



which the proposed framework improves snow density mapping in terms of spatiotemporal representation beyond the reanalysis product.

Finally, we use GlobSnow v3.0 SWE data for an independent application evaluation to examine whether the estimated snow density from NH-SDN improves SWE estimation by comparing with products that assume a fixed snow density (Luojus et al., 2021).

Table 2. Input features for the SDN-Net model.

Feature category	Feature	Data source
Snow characteristics	Snow albedo, snow cover fraction, snow density distribution, snow depth, 24h cumulative snowfall, snow pressure, snow surface temperature, Surface albedo	ERA5-Land
	Snow class	NSIDC
Meteorological	2m air temperature, precipitation, surface pressure, 10m northward wind, 10m eastward wind, soil surface temperature	ERA5-Land
Vegetation	High vegetation LAI, low vegetation LAI	
Temporal	Day of hydrological year	-
	Solar declination, latitude, angular speed	-
Spatial	Longitude, latitude	-
Topographic	Elevation, slope, aspect	GMTED2010 DEM

https://doi.org/10.5194/essd-2026-689
Preprint. Discussion started: 2 November 2026
© Author(s) 2026. CC BY 4.0 License.

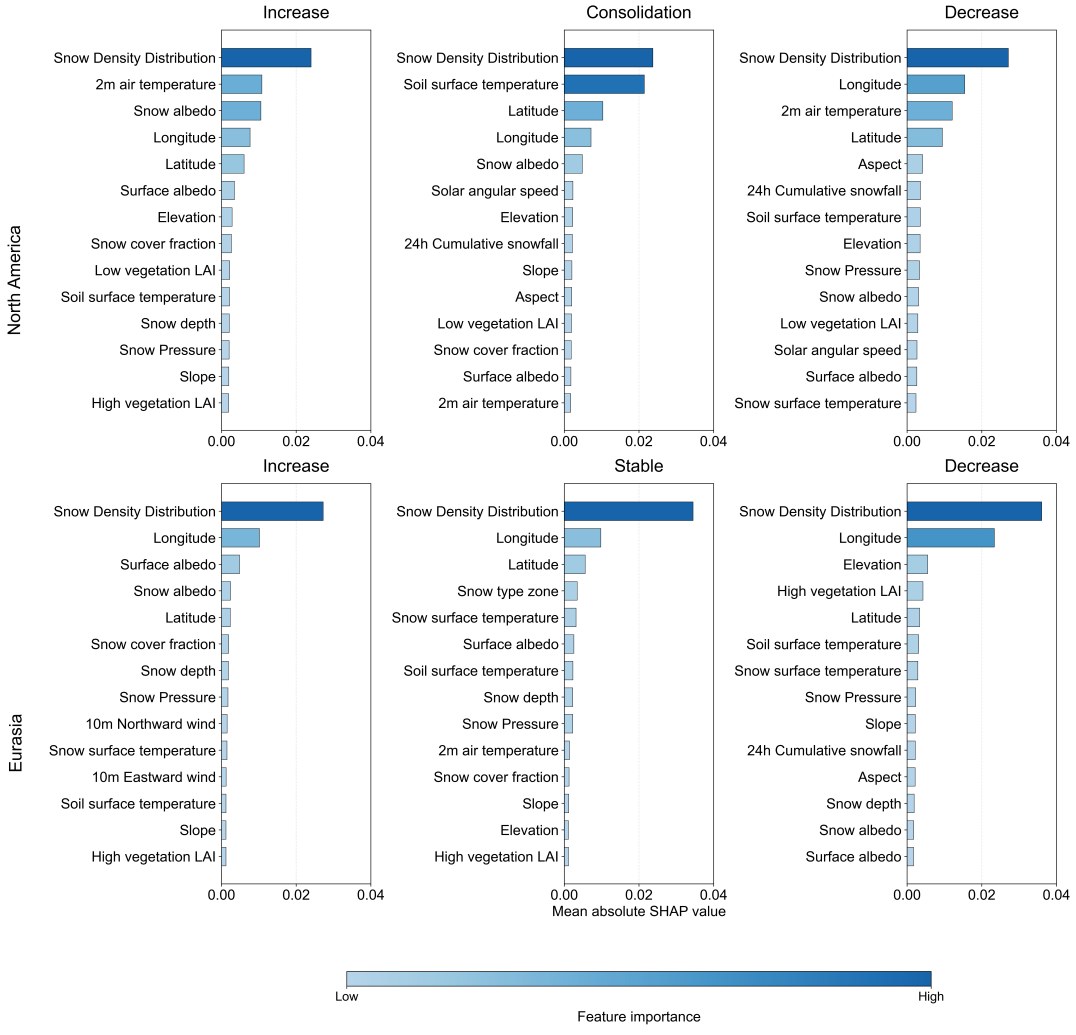
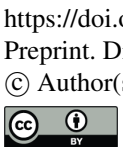


Figure 2. Feature importance across snow density evolution stages derived from SHAP analysis.

3 Methodology

The workflow for generating the dataset consists of three stages: (1) data preparation and sample construction, (2) model training and performance comparison, and (3) generation and evaluation of the product, as shown in Fig.3. The overall framework is designed to bridge the gap between sparse and unevenly distributed in-situ snow density observations and the need for spatially continuous, long-term estimates across the Northern Hemisphere. In the first stage, snow density measurements are spatially and temporally matched with environmental conditions to construct training samples and labels. In the second stage, the model learns the relations between snow density and its spatiotemporal controls, and its spatial and

https://doi.org/10.5194/essd-2026-689
Preprint. Discussion started: 2 November 2026
© Author(s) 2026. CC BY 4.0 License.



Open Access Earth System Science Data Discussions

temporal extrapolation capabilities are evaluated. In the third stage, the learned relations are extended across the full spatiotemporal domain, and the reliability of the resulting snow density product is further assessed using reanalysis data.

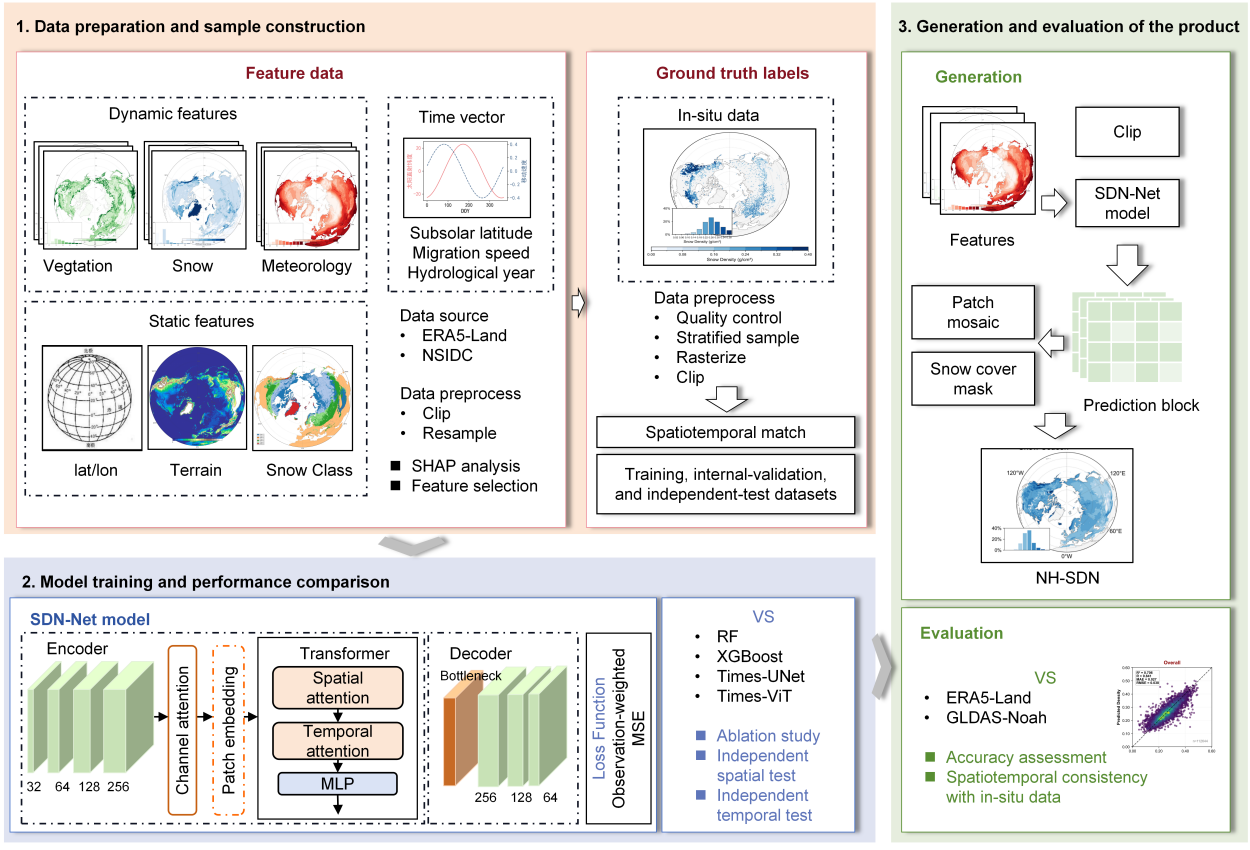


Figure 3. Overall workflow for NH-SDN development, from multisource data integration and model construction to large-scale snow density mapping and product evaluation.

3.1 Data preparation and sample construction

Snow density mapping requires the integration of sparse in-situ observations with spatially continuous environmental information. We spatially harmonize all input datasets to a common 0.25° grid through reprojection and resampling to ensure consistency among in-situ observations, reanalysis variables, and auxiliary geographic data. The modelled domain comprises Northern Hemisphere land areas, excluding grid cells classified as ICE in the global seasonal snow classification of Sturm and Liston (2021) after resampling to the common 0.25° grid. The ICE class identifies glaciers and ice sheets, which are outside the seasonal snow domain targeted by NH-SDN. Snow persisting across years can evolve into firn, with density

https://doi.org/10.5194/essd-2026-689
Preprint. Discussion started: 2 November 2026
© Author(s) 2026. CC BY 4.0 License.


characteristics distinct from seasonal snow (Zhao et al., 2023). We therefore exclude ICE-classified grid cells rather than extend the seasonal snow density reconstruction to these environments.

The modeled domain is then divided into 256×256 patches with a 20% overlap to facilitate model training and large-scale inference. For model development and final evaluation, patches containing in-situ snow density observations are used to construct training, internal-validation, and independent-test datasets following the temporal and spatial holdout procedures described in Section 3.3. The training datasets are used to optimize model parameters, while the internal-validation datasets are used to monitor model performance and select model checkpoints. The independent-test datasets are reserved exclusively for final evaluation after model configuration and checkpoint selection and are not used for model selection, hyperparameter tuning, or early stopping. The in-situ measurements within each data subset are rasterized onto the 0.25° grid and used as regression targets. When multiple observation sites within the same subset are located in the same grid cell on the same day, their measurements are averaged to obtain a representative target value, ensuring that each grid cell–day combination corresponds to a unique regression target.

We organize dynamic environmental variables, including snow, meteorological, and vegetation factors, into spatiotemporal cubes. For each sample, we stack observations from the current day and the preceding three days along the temporal dimension to characterize short-term changes in snowpack conditions and their meteorological forcing, which jointly regulate snow density evolution. We treat static variables, including snow class, elevation, and other geographic factors, as spatial auxiliary data and normalize them using min–max scaling before model training. To represent seasonal snow evolution, we generate temporal encoding variables according to the observation date within each hydrological year. We subsequently integrate dynamic, static, and temporal variables as inputs to the SDN-Net framework.

3.2 SDN-Net model

SDN-Net takes dynamic environmental variables, static geographic features, and time vectors as inputs to characterize the spatial heterogeneity, temporal evolution, and environmental controls of snow density. It adopts a hybrid ViT–CNN architecture consisting of two parallel encoder branches, namely the CNN Local Branch and the Transformer Branch, followed by a CNN-based decoder for snow density estimation (Fig. 4). The CNN Local Branch extracts hierarchical spatial features through progressive downsampling. In parallel, the Transformer Branch first applies 5D soft distribution calibration to recalibrate heterogeneous environmental features while preserving their spatiotemporal structures. Channel attention is then used to adjust the importance of different input variables during different snowpack evolution stages. The refined features are processed by a Space-Time Transformer to capture global spatiotemporal dependencies of snow density variations. The Static-Time FiLM module further incorporates geographic and temporal information to refine the Transformer features. The CNN decoder progressively restores spatial resolution through upsampling and integrates features from the two encoder branches. Finally, the Dense Regression Head generates continuous snow density maps, and the model is trained using the observation-weighted mean squared error loss.

https://doi.org/10.5194/essd-2026-689
Preprint. Discussion started: 2 November 2026
© Author(s) 2026. CC BY 4.0 License.

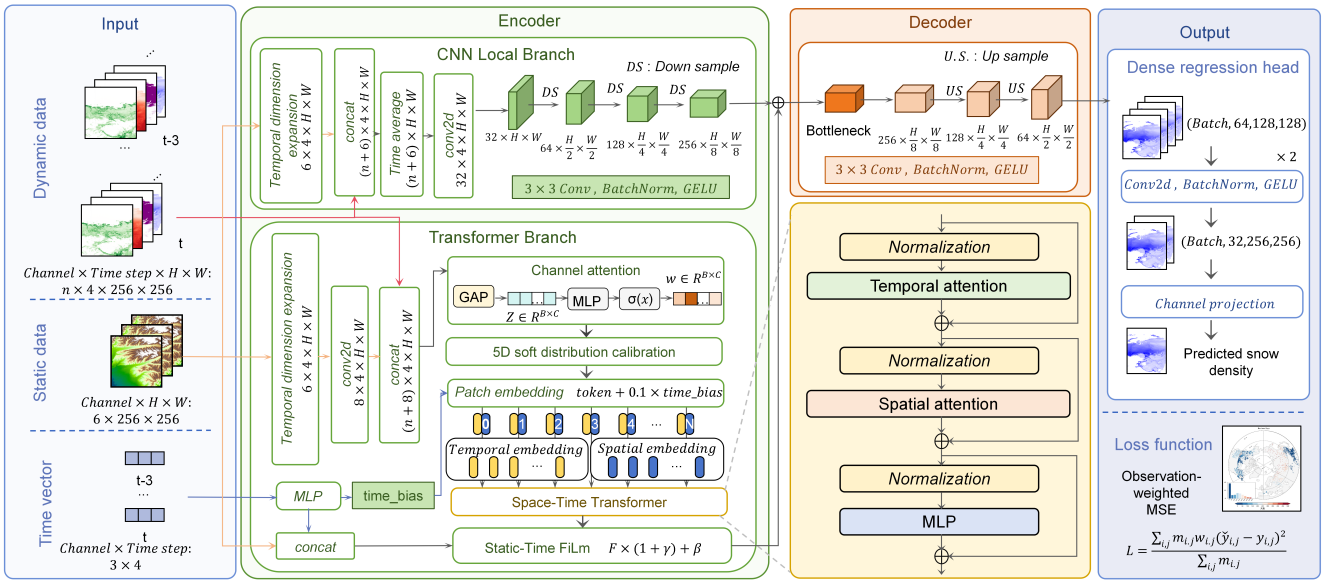


Figure 4. Overall architecture of SDN-Net for learning spatiotemporal snow density variations from multisource environmental information.

3.2.1 Input representation

Inputs are embedded into different pathways within the network. Snow density evolution is jointly controlled by environmental, geographic, and temporal factors. The dynamic environmental variables include snow, meteorological, and vegetation-related variables. They are organized as spatiotemporal cubes by stacking four consecutive time steps to represent short-term environmental changes. The static geographic features include elevation, slope, aspect, latitude–longitude information, and snow classes, providing spatial constraints for snow density estimation. Dynamic and static features are jointly incorporated into both encoder branches. In the CNN Local Branch, static features are temporally expanded and concatenated with dynamic variables to extract spatial representations through convolutional layers. In the Transformer Branch, static features are projected into latent representations and fused with dynamic variables to construct spatiotemporal feature tensors for tokenization.

The time vectors provide additional temporal context for snow evolution and include the day in a hydrological year, solar declination, latitude, and moving speed. They are embedded through a multilayer perceptron (MLP) to generate time biases, which are added to patch tokens during token construction. Static features and time vectors are further combined in the Static-Time FiLM module to generate adaptive modulation parameters for refining Transformer features.

https://doi.org/10.5194/essd-2026-689
Preprint. Discussion started: 2 November 2026
© Author(s) 2026. CC BY 4.0 License.



3.2.2 Transformer branch encoder

The Transformer Branch integrates dynamic environmental variables, static geographic features, and temporal information to characterize spatiotemporal variations in snow density. The Channel Attention and 5D soft distribution calibration modules enhance informative features and improve the consistency of heterogeneous inputs, while the Space-Time Transformer captures long-range dependencies among environmental conditions and snow density evolution.

The 5D soft distribution calibration module is used to adjust the distributions of heterogeneous environmental variables while preserving their spatiotemporal patterns. This operation improves the consistency of multi-source environmental features and provides more reliable representations for snow density estimation.

The Channel Attention module dynamically recalibrates the importance of environmental variables across different snow density evolution stages, allowing the network to adaptively emphasize stage-specific controlling factors. It is applied to the fused dynamic and static feature maps prior to patch embedding, where it generates channel-wise weights to enhance informative representations. Given a feature map $X \in R^{B\times C\times T\times H\times W}$, the channel attention generates a weighting vector $w \in R^{C}$ through global average pooling and a small feed-forward network:

$$w=\sigma\left(\mathrm{MLP}\left(\mathrm{GAP}(x)\right)\right), \quad (3)$$

where σ denotes the sigmoid activation and GAP denotes global average pooling across the spatial and temporal dimensions (Hu et al., 2020). The recalibrated feature map is obtained by applying these channel-wise weights to the original feature map. This mechanism enables adaptive recalibration of environmental representations across different snow density evolution stages, providing additional flexibility for modeling stage-dependent snow density variations.

The calibrated feature tensor is converted into token representations through patch embedding. Specifically, each spatial patch is flattened and projected into a D-dimensional embedding space through a learnable linear mapping:

$$z_i=Wx_i+b_i, \quad (4)$$

where z_i denotes the token representation of the patch, x_i represents the flattened feature vector, W and b_i denote the learnable projection weights and bias. The tokens are used as inputs for the Space-Time Transformer.

The time vectors provide additional temporal context for snow evolution. They are embedded through MLP to generate time biases, which are added to patch tokens during token construction:

$$z_i^{'}=z_i+0.1\times \mathrm{time_bias}, \quad (5)$$

where $z_i^{'}$ represents the token representation with temporal information, and time_bias denotes the temporal embedding generated from the time vectors. We test different values for this coefficient and find that 0.1 gives the best results. It adds useful seasonal information without overpowering the environmental features.

The tokens are processed by the Space-Time Transformer. This module adopts a ViT-based architecture with decoupled temporal and spatial attention mechanisms to capture temporal evolution and spatial variation in snow density (Bertasius et al., 2021). Before Transformer encoding, learnable spatiotemporal positional embeddings are added:

https://doi.org/10.5194/essd-2026-689
Preprint. Discussion started: 2 November 2026
© Author(s) 2026. CC BY 4.0 License.



Open Access Earth System Science Data Discussions

$$Z^0=Z+E_{pos}, \quad (6)$$

where Z^0 denotes the initial token representations, Z represents the input token sequence, and E_{pos} denotes learnable positional embeddings encoding spatial and temporal locations.

Within each Transformer block, temporal attention is applied among tokens corresponding to the same spatial location across different time steps:

$$A_t=\text{softmax}(\frac{Q_tK_t^T}{\sqrt{d}}), \quad (7)$$

where A_t denotes the temporal attention matrix, Q_t and K_t represent the query and key matrices for temporal attention, and d denotes the feature dimension. Temporal attention aggregates information across consecutive days to capture short-term changes in snow and meteorological conditions associated with snow accumulation, densification, and melt.

$$A_s=\text{softmax}(\frac{Q_sK_s^T}{\sqrt{d}}), \quad (8)$$

where A_s denotes the spatial attention matrix, Q_s and K_s represent the query and key matrices for spatial attention. Spatial attention captures interactions among different locations and improves the representation of regional differences in snow density associated with terrain, climate, and snow regimes.

Through sequential temporal and spatial attention operations, the Space-Time Transformer captures temporal evolution and spatial variability in snow density. The resulting representations are refined by the Static-Time FiLM module using static geographic information and time vectors, which are encoded to generate feature-wise modulation parameters:

$$F'=F\times(1+\gamma)+\beta, \quad (9)$$

where F and F' denote the Transformer feature representations before and after modulation, γ and β epresent the feature-wise scaling and shifting parameters. This modulation introduces geographic constraints and seasonal context into high-level representations, improving the characterization of spatial differences and temporal variations in snow density.

Finally, the refined Transformer features are reshaped and transferred to the CNN decoder for spatial reconstruction and dense snow density regression.

3.2.3 CNN local branch encoder and CNN-based local decoder

The CNN Local Branch aggregates the temporal dimension of the input spatiotemporal cubes through temporal averaging and then extracts hierarchical spatial representations using convolutional blocks. Specifically, the shallow encoder consists of sequential convolutional layers with batch normalization and GELU activation, which progressively increase feature channels and reduce spatial resolution through downsampling. These multi-scale representations preserve fine-grained spatial variations in environmental conditions that contribute to local snow density heterogeneity.

https://doi.org/10.5194/essd-2026-689
Preprint. Discussion started: 2 November 2026
© Author(s) 2026. CC BY 4.0 License.



The CNN-based local decoder reconstructs spatially continuous snow density fields by progressively recovering spatial resolution and fusing Transformer representations with local features extracted by the CNN encoder. Specifically, the Transformer patch embeddings are first projected through a bottleneck convolutional block to reduce channel dimensionality while preserving spatial structures. The projected features are progressively upsampled through sequential convolutional layers with batch normalization and GELU activation, and fused with encoder features at corresponding spatial scales through skip connections. This process enables the reconstruction of local spatial details in snow density, which is particularly important in complex and fragmented terrains.

Finally, the refined decoder features are passed to the dense regression head, which uses convolutional refinement layers and a 1×1 convolutional projection to generate a single-channel continuous snow density map.

3.2.4 Loss function with observation-weighted MSE

In-situ snow density records are highly uneven in their temporal coverage, so SDN-Net employs an observation-weighted mean squared error (MSE) loss, which assigns higher weights to pixels with longer in-situ observation records. This weighting strategy is based on the assumption that locations with more observation days provide more reliable and representative snow density information, and therefore should contribute more to model optimization.

For each valid pixel, the squared error between the predicted value $\hat{y}_{i,j}$ and the ground truth $y_{i,j}$ is scaled by a weight derived from the normalized observation count:

$$w_{i,j}=1+\sigma\cdot\text{normalized}(c_{i,j}), \tag{10}$$

where $c_{i,j}$ is the number of days the pixel has been observed, and σ controls the maximum contribution of highly observed pixels. The final loss is computed by applying this weight to the squared error over all valid pixels:

$$L=\frac{1}{\sum m_{i,j}}\sum_{i,j} m_{i,j}w_{i,j}(\hat{y}_{i,j}-y_{i,j}), \tag{11}$$

where $m_{i,j}$ is a mask indicating valid pixels. In the implementation, σ is set to 0.3, meaning that the loss contribution of the pixels with the highest number of observations increases by up to 30% relative to pixels with minimal observations. By weighting the loss in this manner, the network is guided to focus on regions with reliable and frequent measurements, while reducing the influence of sparse or noisy observations.

3.2.5 Experimental setup

We train separate models for North America and Eurasia because the dominant controls on snow density differ between the two continents. The main factors governing snow density variations within the hydrological year also differ between the two continents (Fig. 1 and Fig. 2). The two models share the same architecture and training strategy, but use region-specific input variables selected according to their dominant environmental controls and are trained with observations from their respective

https://doi.org/10.5194/essd-2026-689
Preprint. Discussion started: 2 November 2026
© Author(s) 2026. CC BY 4.0 License.



regions. The models are trained on four NVIDIA RTX 3090 GPUs, with a mini-batch size of 2 per GPU. For the Tibetan Plateau and Xinjiang, the Eurasia model is further fine-tuned using the regional development data defined in Section 3.3.

During model development, all models are trained for 35 epochs without early stopping. Checkpoints are selected based on the lowest internal-validation loss defined in Section 3.2.4, reached at epochs 16, 32, and 20 for North America, Eurasia, and regional fine-tuning, respectively.

For final dataset production, the models are retrained from their original initialization on the combined training and internal-validation data using the selected hyperparameters and training durations. Table 3 summarizes the training settings and elapsed time to the selected epochs.

Table 3. Training settings and elapsed time to the selected epochs for the models and regional fine-tuning.

Parameter	North America	Eurasia	Tibetan Plateau and Xinjiang
Optimizer	AdamW	AdamW	AdamW
Initial learning rate	1×10^{-4}	1×10^{-4}	5×10^{-5}
Weight decay	1×10^{-4}	1×10^{-4}	1×10^{-4}
AdamW β_1, β_2	0.9, 0.999	0.9, 0.999	0.9, 0.999
Learning-rate decay	×0.1 after epochs 8	×0.1 after epochs 8	×0.1 after epochs 8
Maximum gradient norm	1.0	1.0	1.0
Training time to selected epoch (h)	9.6	4.0	2.6

3.3 Dataset generation and evaluation

We apply the trained SDN-Net model to estimate daily snow density across the Northern Hemisphere from 1982 to 2025. All environmental inputs are processed following the same procedure as the training data. Inference is performed on all available patches across the Northern Hemisphere to generate spatially continuous snow density estimates. For each patch, snow density predictions are retained only for snow-covered pixels identified using the ERA5-Land snow cover fraction, with a threshold of 30% applied to define snow-covered areas. This mask excludes snow-free regions from the final estimates. Predictions from adjacent patches are merged by averaging values in overlapping regions, with edge feathering applied to reduce boundary artifacts. The resulting mosaics provide a continuous 0.25° daily snow density dataset covering the Northern Hemisphere from 1982 to 2025. We additionally quantify uncertainty for each valid grid cell and day using a five-member ensemble trained with different random seeds, with the methodology and results presented in Appendix C.

Multiple evaluation strategies are employed to evaluate the reliability of SDN-Net using independent in-situ observations and benchmark models. We compare SDN-Net with four representative approaches: Random Forest (RF), Extreme Gradient Boosting (XGBoost), a time-series U-shaped convolutional neural network (Times-UNet), and a time-series Vision

https://doi.org/10.5194/essd-2026-689
Preprint. Discussion started: 2 November 2026
© Author(s) 2026. CC BY 4.0 License.



Transformer (Times-ViT). RF has been applied to snow density modelling previously (Sun et al., 2024a), while XGBoost represents a point-based machine learning method. Both estimate snow density from predictor variables at individual locations without explicitly considering spatial context. Times-UNet and Times-ViT use the same spatiotemporal input cubes as SDN-Net but adopt different feature extraction mechanisms: Times-UNet captures local and multi-scale patterns through convolutional encoding and decoding, whereas Times-ViT models long-range spatial and temporal dependencies through self-attention. Differently, SDN-Net further combines Transformer-based global modeling with CNN-based local reconstruction, together with feature refinement modules including channel attention to improve representation flexibility.

We use two complementary holdout experiments to assess the temporal and spatial generalization capabilities of the generated NH-SDN dataset. For the temporal holdout experiment, observations from six designated years (1979, 1987, 1995, 2003, 2011, and 2019) are reserved as an independent test set, while time points from the remaining years are divided into training (90%) and internal-validation (10%) subsets. For the spatial holdout experiment, we select development sites using a constrained Latin Hypercube Sampling (cLHS) strategy with a target optimization framework (Mulder et al., 2013), ensuring representative coverage across different snow classes and terrain types while maintaining spatial and temporal uniformity. The sites selected by cLHS constitute the development subset, and all remaining sites are reserved as the independent-test subset. The development sites are further divided into training (90%) and internal-validation (10%) subsets before sample generation. All three subsets share the same dates and input patch windows, but their observation-target masks are constructed separately according to station membership. The independent-test observations are completely excluded from the training and internal-validation targets, preventing leakage of held-out observation labels. The independent spatial test sites are also used for the subsequent evaluation of product accuracy and spatiotemporal consistency. Data partition sizes and the spatial distribution of observation sites are provided in Appendix A (Table A1 and Fig. A1).

The consistency of the model outputs is further assessed by comparing the SDN-Net predictions and reanalysis data with in-situ observations. On one hand, temporal consistency is quantified using the Consistency Index (CI) (Yan et al., 2024), defined as:

$$CI=\frac{N_{inc}+N_{dec}+N_{no}}{N_{tot}}, \tag{12}$$

where N_{inc}, N_{dec}, N_{no} represent the number of grid cells where both datasets exhibit a significant increasing trend, a significant decreasing trend, or no significant trend, respectively, and N_{tot} is the total number of grid cells. On the other hand, spatial consistency is quantified using the Taylor Skill Score (TSS) (Taylor, 2001):

$$TSS=\frac{4(1+R)^4}{(STDR+STDR_{obs})^2(1+R_0)^4}, \tag{13}$$

where R is the Pearson correlation coefficient between model and observations, STDR and $STDR_{obs}$ are the standard deviations of model and observed fields, and $R_0=1$ is the maximum attainable correlation (Li et al., 2026). These metrics allow assessment of both the temporal trends and spatial patterns of snow density.

https://doi.org/10.5194/essd-2026-689
Preprint. Discussion started: 2 November 2026
© Author(s) 2026. CC BY 4.0 License.



4 Results

4.1 Model performance evaluation

4.1.1 Accuracy comparison with other models

We compare the performance of multiple models for estimating snow density against in-situ station observations across North America and Eurasia. SDN-Net consistently achieves the highest overall accuracy across almost all test settings (Fig. 5). In the independent spatial test, SDN-Net achieves an R^2 of 0.579 in North America, outperforming other models. Its performance is even better over Eurasia (R^2 = 0.646, MAE = 0.029 g cm^{-3}), surpassing the single time-point and single spatial-point prediction models, such as RF (R^2 = 0.565) and XGBoost (R^2 = 0.564), as well as Times-UNet (R^2 = 0.634) and Times-ViT (R^2 = 0.604). These results demonstrate that the hybrid model combining ViT and CNN, which accounts for spatial contextual information, possesses stronger spatial prediction capability. In the independent temporal test, SDN-Net achieves an R^2 of 0.652 in North America and 0.694 in Eurasia, outperforming other models, demonstrating its strong temporal prediction capability.

https://doi.org/10.5194/essd-2026-689
Preprint. Discussion started: 2 November 2026
© Author(s) 2026. CC BY 4.0 License.

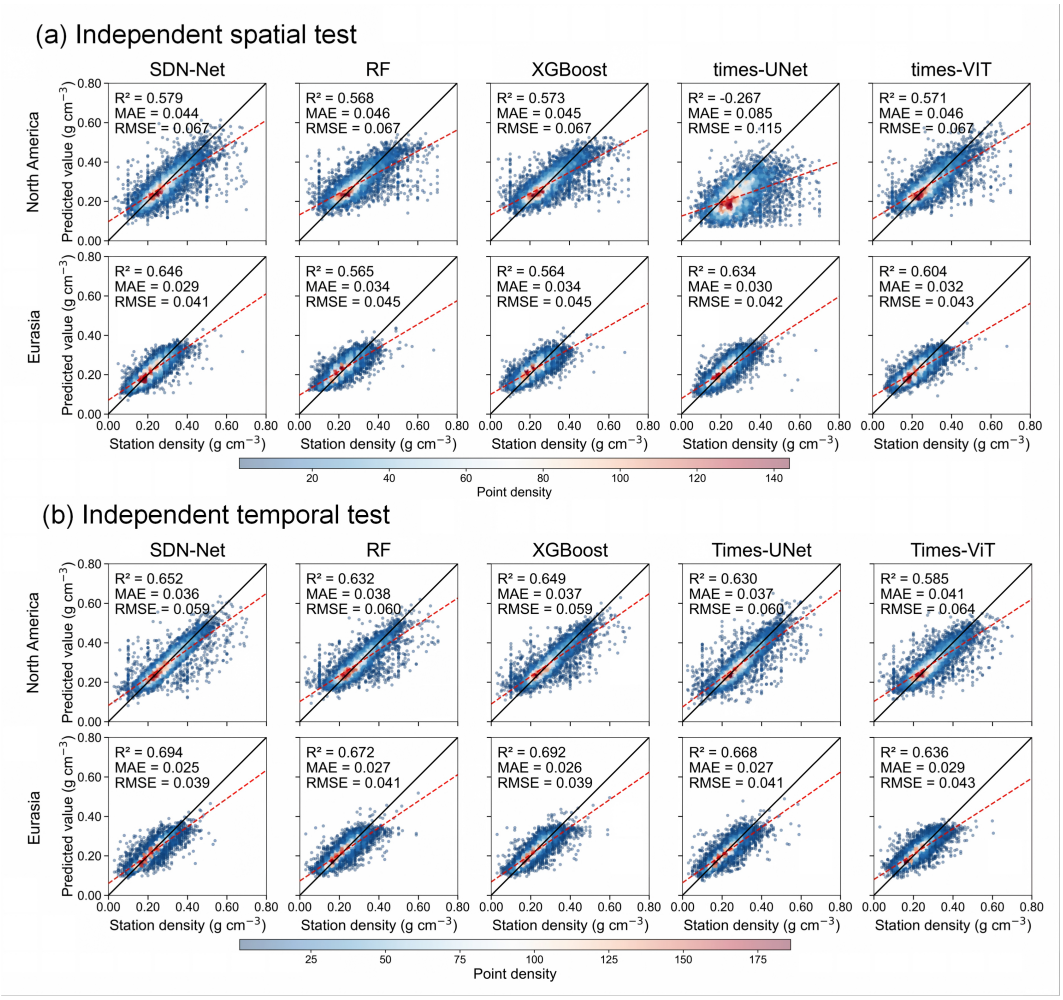


Figure 5. Independent evaluation of snow density predictions from different models against in-situ observations across North America and Eurasia. (a) Independent spatial test and (b) independent temporal test results for five models. Scatter points represent predicted and observed snow density pairs, with colors indicating point density. Black lines indicate the 1:1 relation, and red dashed lines show linear regression fits. Model performance is evaluated using R^2, MAE, and RMSE, with MAE and RMSE expressed in g cm^{-3}.

4.1.2 Effectiveness of features and model architecture

We design ablation experiments by comparing different input data and model architectures (Table 3) to systematically evaluate the effectiveness of each key component of SDN-Net. Regarding the input data, removing snow, meteorological data, vegetation data, and static features and time vectors each leads to a significant decline in model performance. These results demonstrate that every type of feature provides unique and valuable information for accurate prediction. Among these,

https://doi.org/10.5194/essd-2026-689
Preprint. Discussion started: 2 November 2026
© Author(s) 2026. CC BY 4.0 License.



the absence of meteorological data causes the most severe degradation, with RMSE increasing from 0.0525 to 0.2384 g cm^{-3}. At the model component level, removing the CNN Decoder increases RMSE to 0.0578 g cm^{-3} and decreases R^2 to 0.5912, demonstrating that the decoder plays a crucial role in feature reconstruction and spatial information preservation. Removing the observation-weighted MSE loss function leads to a slight increase in both RMSE and MAE, with R^2 dropping to 0.6426, confirming the effective guidance of this loss function toward the optimization objective.

Table 3. Ablation study of SDN-Net, showing the impact of input data and model architecture on predictive performance.

Class	Method	R^2	MAE (g cm^{-3})	RMSE (g cm^{-3})
	SDN-Net	0.6634	0.0344	0.0525
Input Data	w/o snow	0.0343	0.0645	0.0888
	w/o meteorology	−5.9534	0.1939	0.2384
	w/o vegetation	−3.0629	0.1447	0.1822
	w/o static feature and time vector	−0.1417	0.0751	0.0966
Model architecture	w/o CNN Decoder	0.5912	0.0406	0.0578
	Standard MSE	0.6426	0.0366	0.0541
	w/o Channel Attention	0.6624	0.0347	0.0526
	w/o Static-Time FiLM	0.6622	0.0345	0.0526

4.2 Comparison with reanalysis snow density

NH-SDN is benchmarked against GLDAS-Noah and ERA5-Land using the independent spatial test sites defined in Section 3.3. The evaluation considers both prediction accuracy and spatiotemporal consistency with in-situ observations. Accuracy is examined across different months, snow classes, and elevation ranges, while temporal and spatial consistency is assessed in terms of seasonal evolution, interannual variability, and regional spatial patterns. Together, these analyses provide a multidimensional assessment of the performance of NH-SDN relative to the two reanalysis products.

4.2.1 Accuracy assessment

We compare the accuracy of daily snow density across different months, as well as the monthly-mean snow density across snow classes and elevation. Overall, NH-SDN consistently outperforms the other datasets across all months and regions. Meanwhile, its accuracy still exhibits clear variability across different temporal and environmental conditions (Fig. 6). From December to May of the following year, NH-SDN consistently outperforms GLDAS-Noah and ERA5-Land, with the lowest

https://doi.org/10.5194/essd-2026-689
Preprint. Discussion started: 2 November 2026
© Author(s) 2026. CC BY 4.0 License.


RMSE of 0.05 g cm^{-3} in January. The seasonal variations in product performance are closely associated with snow amount and snowpack stability. All three products show a similar pattern of accuracy decreasing and then increasing throughout the snow season, while NH-SDN consistently achieves higher accuracy than the two reanalysis products. During the increase stage, NH-SDN still achieves an R of 0.539, considerably higher than GLDAS-Noah (0.374) and ERA5-Land (0.228). Notably, compared with the increase stage, reanalysis products show larger errors during the decrease stage, which may be related to the increase of uncertainties in process-model simulations. In contrast, NH-SDN maintains stable performance during snowmelt, with RMSE values substantially lower than those of the reanalysis products, demonstrating its advantage in capturing snow density variations under complex snow conditions.

In terms of snow classes, NH-SDN maintains consistently high performance across all snow classes, with R values ranging from 0.796 to 0.883, demonstrating its applicability across diverse snow classes. It performs particularly well in maritime regions (R = 0.883) and montane forest regions (R = 0.854), indicating strong capability in capturing snow density variations under deep snow and relatively humid conditions. In contrast, reanalysis-based datasets exhibit larger inter-class variability, with reduced accuracy in data-scarce regions such as tundra.

In terms of elevations, NH-SDN maintains consistently high accuracy across all elevation bands, with R values ranging from 0.813 to 0.900, demonstrating robustness to topographic heterogeneity. In comparison, both reanalysis products perform well mainly at elevations below 2 km but show substantially lower accuracy at higher elevations, highlighting the advantage of NH-SDN in complex high-elevation regions.

https://doi.org/10.5194/essd-2026-689
Preprint. Discussion started: 2 November 2026
© Author(s) 2026. CC BY 4.0 License.

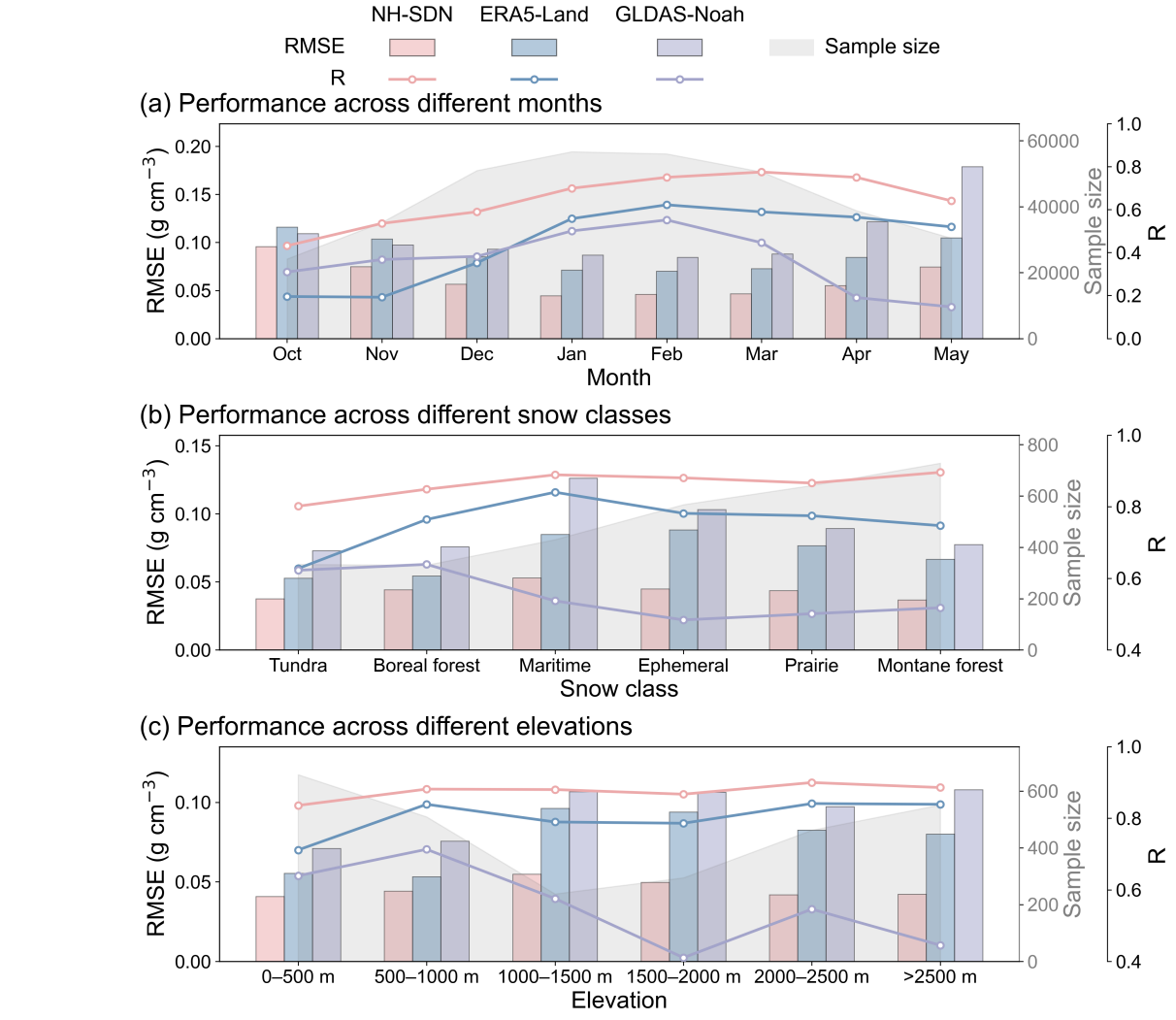


Figure 6. Evaluation of NH-SDN and reanalysis datasets (ERA5-Land and GLDAS-Noah) against in-situ observations using daily and monthly-mean snow density predictions. Bars denote RMSE, lines denote R values, and shaded areas indicate sample sizes. (a) Monthly variations in daily prediction performance. (b) Prediction performance across different snow classes based on monthly-mean snow density. (c) Prediction performance across different elevation zones.

4.2.2 Temporal and spatial variability evaluation

Comparison of the temporal consistency between NH-SDN, reanalysis products, and in-situ observations shows that NH-SDN effectively mitigates the systematic underestimation commonly observed in reanalysis datasets, particularly over North America (Fig. 7b). Reanalysis products substantially underestimate snow density during both the increase and decrease

https://doi.org/10.5194/essd-2026-689
Preprint. Discussion started: 2 November 2026
© Author(s) 2026. CC BY 4.0 License.


periods in North America, whereas NH-SDN, benefiting from extensive North American observations for model training, largely alleviates this bias. Consequently, the CI increases from 0.48 for ERA5-Land and 0.41 for GLDAS-Noah to 0.62. NH-SDN demonstrates superior temporal consistency and higher agreement with ground-based observations across all snow classes at the seasonal scale. Following snow stabilization in December, NH-SDN substantially mitigates the underestimation of snow density in reanalysis data, particularly in montane forest and prairie regions (Fig. 7b). During the snowmelt period in tundra and boreal forest, GLDAS-Noah tends to overestimate snow density, whereas NH-SDN aligns more closely with in-situ measurements. In terms of annual means and interannual trends, NH-SDN shows better agreement with in-situ observations, notably reducing the underestimation in reanalysis data after 2005 in maritime and ephemeral zones. In the tundra, both NH-SDN and in-situ observations exhibit increasing trends, while reanalysis products show decreasing trends, primarily due to errors in trend estimation during the consolidation stage across the North American Pan-Arctic region. In montane forests, particularly along the western cordillera of North America, in-situ data indicate an upward trend, whereas reanalysis products display a spurious downward trend caused by persistent underestimation, especially during the increase and decrease stages. NH-SDN successfully corrects this bias and reproduces the observed increasing trend.

The spatial consistency of NH-SDN is further evaluated against reanalysis products using ground observations (Fig. 7c). NH-SDN substantially reduces the underestimation observed in reanalysis datasets over the western coastal mountains and eastern North America, as well as central and eastern Russia. We calculate the TSS, and the results show that NH-SDN outperforms both reanalysis products over North America and Eurasia to quantitatively assess spatial performance. The improvement is particularly pronounced in North America, where the TSS increases from 0.82 for ERA5-Land and 0.80 for GLDAS-Noah to 0.94. These results indicate that NH-SDN strengthens the spatial agreement with observations, more accurately captures spatial variability, and consistently achieves substantially higher TSS values.

https://doi.org/10.5194/essd-2026-689
Preprint. Discussion started: 2 November 2026
© Author(s) 2026. CC BY 4.0 License.

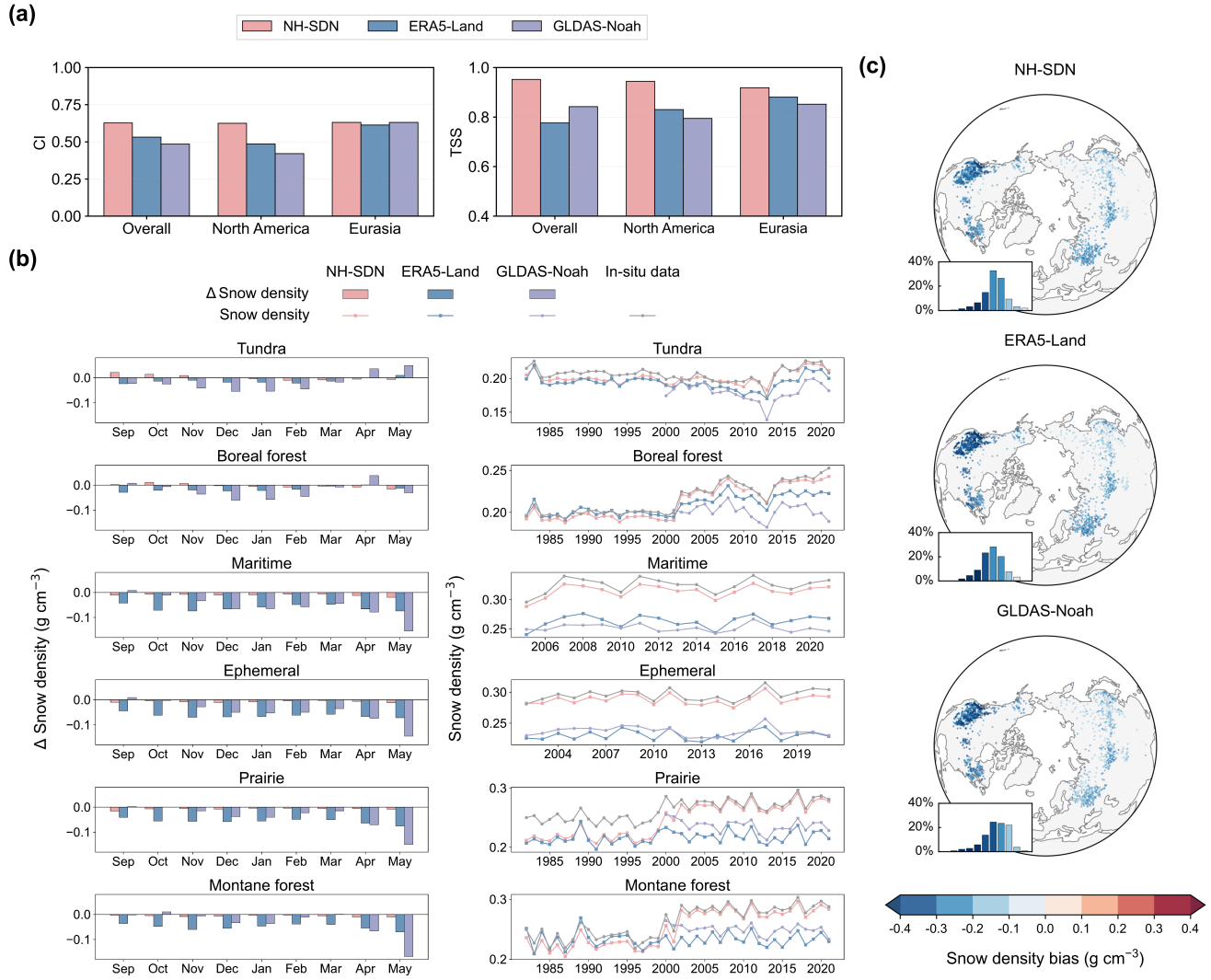


Figure 7. Spatiotemporal consistency evaluation of NH-SDN and reanalysis datasets (ERA5-Land and GLDAS-Noah) against in-situ observations across the Northern Hemisphere. (a) Comparison of consistency index (CI) and Taylor skill score (TSS) among NH-SDN and reanalysis datasets across the Northern Hemisphere, North America, and Eurasia. Bars represent the evaluation metrics calculated against in-situ observations. (b) Monthly biases and interannual variations of snow density across different snow classes. Bars represent monthly mean biases relative to in-situ observations, and lines show the interannual variations of NH-SDN, reanalysis datasets, and in-situ observations. (c) Spatial distribution of mean snow density biases relative to in-situ observations. Colors indicate the magnitude and direction of biases, with blue and red representing underestimation and overestimation, respectively; inset bars show the proportion of grid cells within each bias interval.

https://doi.org/10.5194/essd-2026-689
Preprint. Discussion started: 2 November 2026
© Author(s) 2026. CC BY 4.0 License.



4.3 Long-term snow density mapping

4.3.1 Spatiotemporal distribution

Mean snow density across different evolution stages exhibits pronounced spatial heterogeneity (Fig. 8). Snow density in North America (0.22–0.40 g cm^{-3}) is markedly higher than that in Eurasia (0.12–0.30 g cm^{-3}). Spatially, the regions with high snow density are primarily concentrated in the coastal mountainous areas of western North America and the Rocky Mountains, where snow density ranges from 0.30 to 0.32 g cm^{-3}, substantially exceeding that of central and eastern North America (0.18–0.22 g cm^{-3}). This contrast is mainly associated with the climate–topography coupling effect, as western North America is characterized by maritime snow class, where frequent warm and moist air intrusions generate abundant, relatively dense snowfall. The resulting deep snowpacks further enhance gravitational compaction, leading to higher mean and maximum snow densities (Bormann et al., 2013; Zhao et al., 2023). Within Eurasia, higher snow density is mainly distributed across the Arctic coastal regions of Russia, the Kamchatka Peninsula, and the northern Siberian Plain. In these high-latitude regions, strong cold-air advection leads to lower temperatures and deeper snowpacks, while the increasing overburden pressure within the snowpack further enhances densification, resulting in snow densities of approximately 0.18–0.24 g cm^{-3}. In contrast, Mongolia and China generally exhibit lower snow densities, mostly below 0.18 g cm^{-3}. These regions are dominated by continental or prairie snow class, where limited snowfall and persistent cold, dry conditions produce shallow and weakly consolidated snowpacks. Strong temperature gradients within the snowpack promote constructive metamorphism and the development of low-density depth hoar, thereby reducing regional mean snow density (Che et al., 2025). Temporally, within a hydrological year, snow density increases progressively with the advancement of the snow season. Continuous densification is driven by snow metamorphism, wind compaction, and successive fresh snowfall events. Snow density reaches its seasonal maximum during the spring melt period under repeated freeze–thaw cycles, with the most pronounced increases observed in mountainous regions of western North America and western Eurasia.

The seasonal variations of snow density within a hydrological year differ markedly among snow classes. Overall, snow density in all regions exhibits a gradual increase over time, reaching relatively high values from late winter to spring. In the tundra, snow density remains generally low with limited interannual variability, ranging only between 0.21 and 0.28 g cm^{-3}. The boreal forest shows a pronounced seasonal increase in snow density, with a peak in spring. The maritime snow climate exhibits the highest overall snow density and the most substantial seasonal increase, primarily driven by frequent snowfall events and strong snow metamorphism processes. In contrast, the ephemeral snow shows large fluctuations and relatively unstable sample sizes, but still presents a clear increasing trend during the mid-to-late winter period. Both the prairie and montane forest regions display a consistent densification process, with snow density gradually increasing throughout winter and reaching maximum values prior to the melt season.

https://doi.org/10.5194/essd-2026-689
Preprint. Discussion started: 2 November 2026
© Author(s) 2026. CC BY 4.0 License.

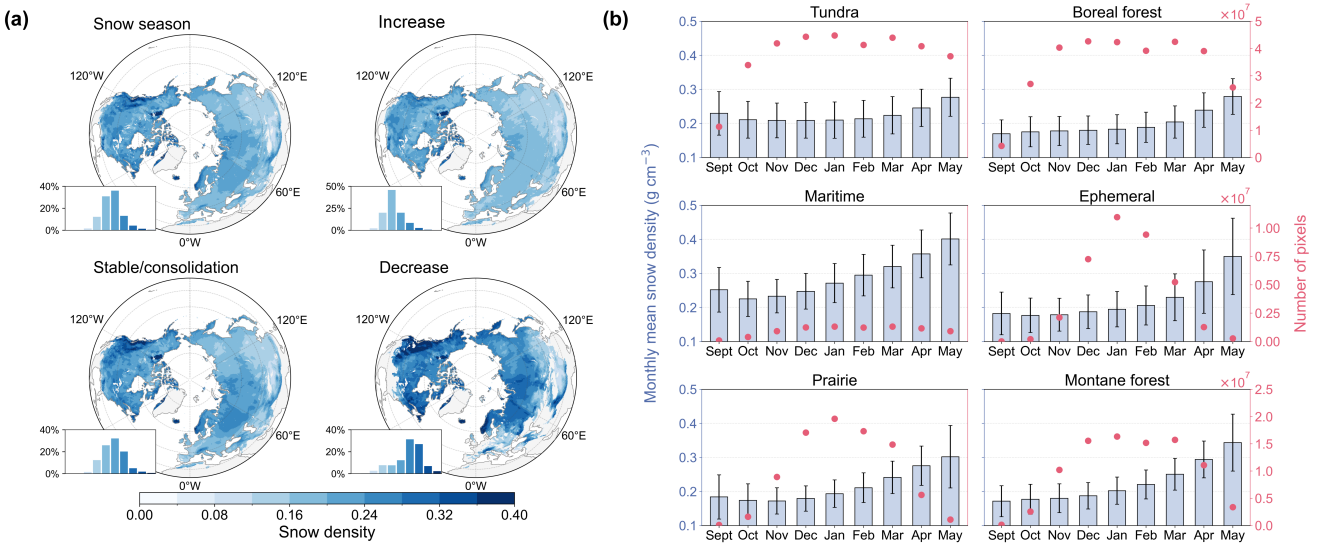


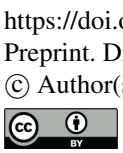
Figure 8. Spatiotemporal variations of multi-year mean snow density across the Northern Hemisphere during different snow density evolution stages and snow classes. (a) Spatial distribution of snow density during the whole snow season and snow density evolution stages. (b) Seasonal variations of snow density across snow classes. Bars represent monthly mean snow density, error bars indicate standard deviations, and dots show pixel counts.

4.3.2 Temporal change

We analyze temporal trends using the non-parametric Mann–Kendall test with Sen's slope estimation. For each grid cell, we first aggregate daily snow density values into annual means for the whole snow season and different snow density evolution stages. We exclude grid cells with fewer than two valid years. We consider trends significant when the Mann–Kendall test and use the corresponding Sen's slope to represent the annual rate of change.

Significant spatial heterogeneity is observed in the annual trends across the whole snow season and different snow density evolution stages. From 1982 to 2025, snow-season-mean snow density over the Eurasian continent exhibits a dominant decreasing trend, with many regions showing a decline exceeding 5×10^{-6} g cm^{-3} yr^{-1}. This decreasing trend in mid- and low-latitude regions may be associated with climate warming, which shortens the snow season. The reduced snow duration and shallower snowpacks weaken long-term compaction processes, leading to lower mean snow density. In contrast, North America displays a mixed pattern of both increasing and decreasing trends. Positive trends are mainly concentrated in high-latitude Eurasia and central North America, where increased warming may enhance the frequency of spring freeze–thaw cycles, promoting snow metamorphism and densification. Whereas negative trends are more widespread, primarily distributed across mid-latitude central and western Eurasia and northern Canada. Most regions in maritime, ephemeral, and prairie snow classes also show decreasing trends.

https://doi.org/10.5194/essd-2026-689
Preprint. Discussion started: 2 November 2026
© Author(s) 2026. CC BY 4.0 License.



Open Access Earth System Science Data Discussions

Seasonally, during the increase stage, increasing trends are observed in the western coastal mountainous regions of North America, while western Russia exhibits decreasing trends. During the decrease stage, high-latitude regions of both Eurasia and central North America show increasing trends. Snow density in tundra and boreal forest regions generally increases, with pronounced increases over the Tibetan Plateau and the consolidation stage in Arctic for tundra, and in the decrease stage over eastern Russia for boreal forest. During the stable stage in Eurasia, the prairie region shows a strong decreasing trend, reaching approximately -1×10^{-5} g cm^{-3} yr^{-1}.

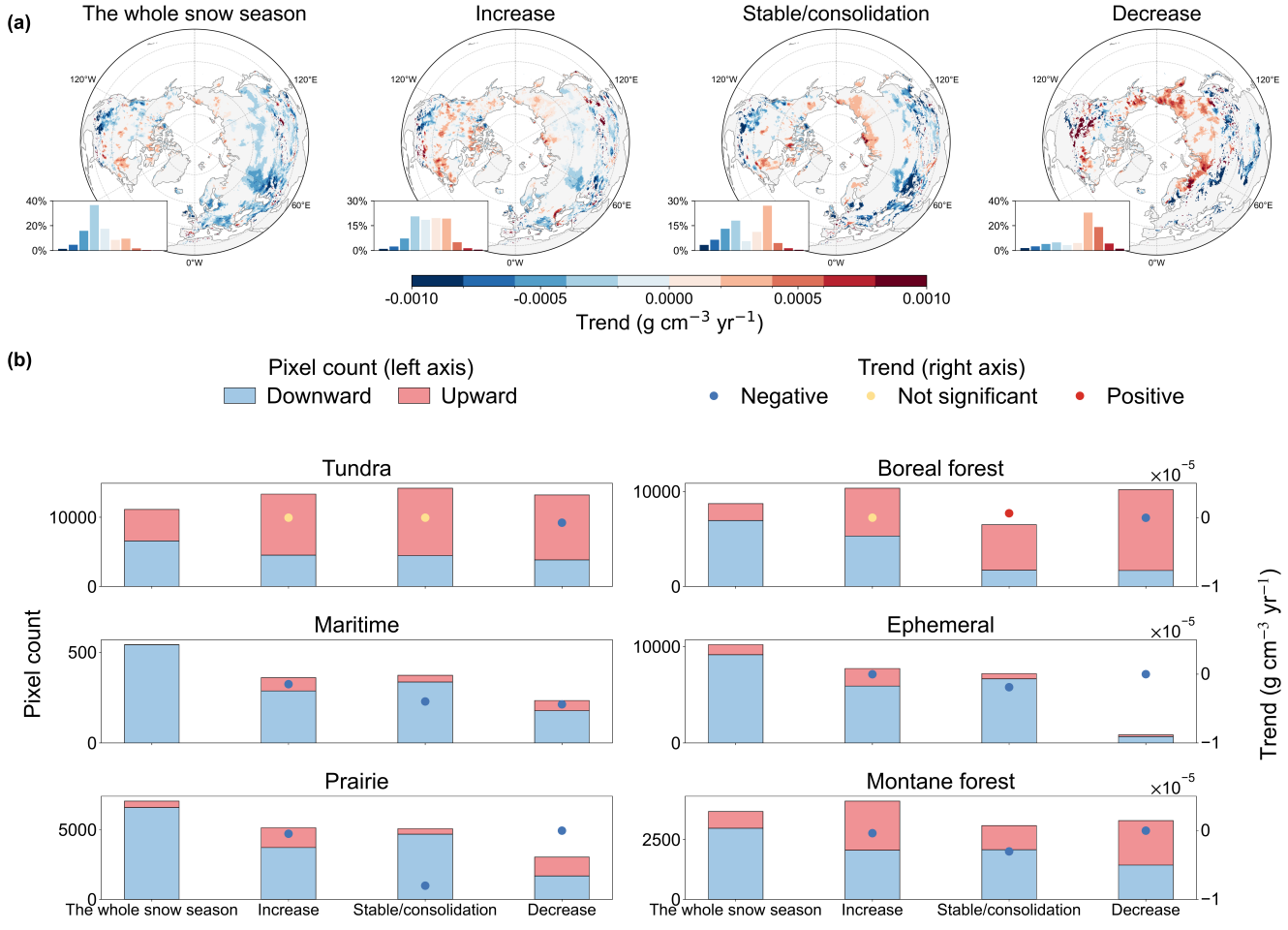


Figure 9. Spatiotemporal patterns of snow density trends across the Northern Hemisphere during 1982–2025. (a) Spatial distribution of snow density trends for the whole snow season and individual snow density evolution stages. Blue and red indicate decreasing and increasing trends, respectively; inset histograms show the percentage distribution of pixel-level trends. (b) Trend variations across snow classes. Stacked bars show pixel counts with downward (light blue) and upward (light red) trends on the left y-axis. Dots show trends in annual mean snow density for the individual evolution stages on the right y-axis (blue: decreasing; red: increasing; yellow: no significant trend).

https://doi.org/10.5194/essd-2026-689
Preprint. Discussion started: 2 November 2026
© Author(s) 2026. CC BY 4.0 License.



4.4 Optimizing SWE products with estimated snow density

Improving SWE products is an important application of daily snow density estimates. The GlobSnow SWE product combines satellite passive microwave observations with ground-based SD observations through a Bayesian assimilation framework to derive SD and then converts it into SWE using a constant snow density of 0.24 g cm^{-3} (Luojus et al., 2021). This fixed-density assumption neglects the spatial and temporal variability of snow density and introduces uncertainties into SWE estimates (Venäläinen et al., 2021). We use NH-SDN to optimize GlobSnow SWE by incorporating spatially and temporally varying snow density information. We recalculate the GlobSnow SWE data by replacing the fixed density assumption with the NH-SDN snow density estimates. The optimized SWE estimates are compared with the original GlobSnow product, and both datasets are validated against in-situ SWE observations to evaluate the contribution of NH-SDN (Fig. 10a). Due to the systematic issue of passive microwave SWE retrievals, which overestimate low values and underestimate high values, and because retrieval sensitivity decreases when SWE exceeds approximately 150 mm, the GlobSnow algorithm tends to provide relatively reliable estimates for moderate snowpacks with SWE below 200 mm, although it mitigates this issue to some extent by assimilating in-situ SD observations. Therefore, in order to focus on evaluating the improvement within the algorithm's effective range, this study selects two thresholds, namely SWE below 500 mm as a broader range and SWE below 200 mm as the effective retrieval range, for accuracy validation and comparative (Venäläinen et al., 2023).

The SWE product optimized with NH-SDN snow density estimates shows improved accuracy (Fig. 10). The correlation coefficient (R) of GlobSnow SWE increases from 0.227 to 0.232 in North America and from 0.719 to 0.772 in Eurasia. The optimized product reduces underestimation and shows a closer agreement with the 1:1 line, demonstrating that daily spatiotemporal snow density estimates improve SWE retrieval accuracy.

We calculate the annual mean SWE distribution before and after optimization to further illustrate the impact of NH-SDN snow density on SWE estimates (Fig. 10b). The multi-year mean GlobSnow SWE is mainly concentrated between 0 and 100 mm, and SWE generally increases with latitude across the Northern Hemisphere. Significant underestimation occurs in North America, particularly along the eastern coast of Canada, where in-situ SWE reaches 160–200 mm while GlobSnow SWE remains at 80–100 mm. In Eurasia, GlobSnow SWE shows moderate underestimation in the mid-latitudes.

After optimization, NH-SDN improves low SWE estimates and better captures spatial variability. Compared with SWE derived from simple interpolation (Venäläinen et al., 2023), the NH-SDN-based product better agrees with in-situ SWE values and spatial patterns, particularly in high-latitude Eurasia. These results highlight the importance of dynamic snow density for improving SWE products.

https://doi.org/10.5194/essd-2026-689
Preprint. Discussion started: 2 November 2026
© Author(s) 2026. CC BY 4.0 License.

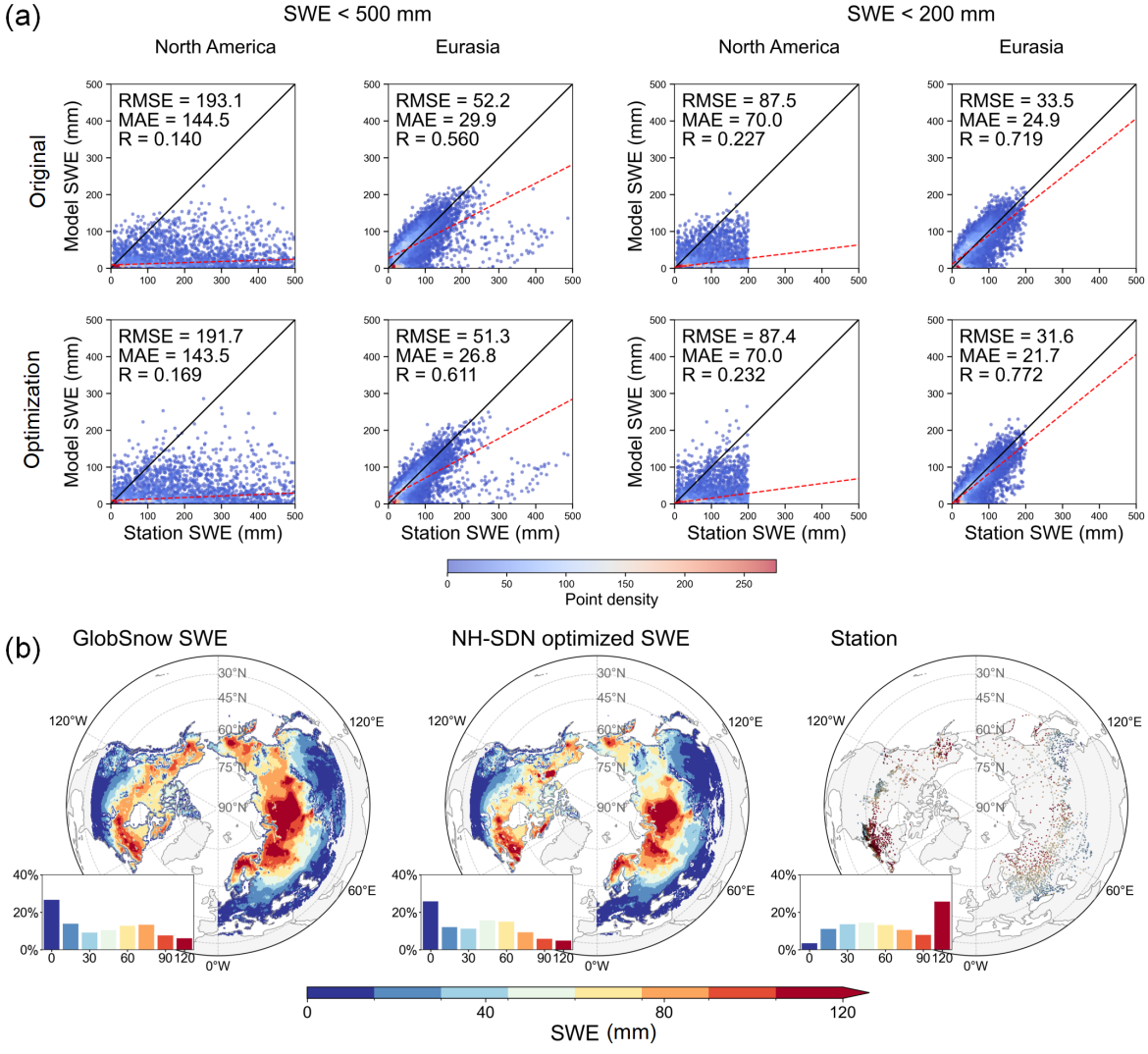


Figure 10. Evaluation of GlobSnow SWE estimates before and after snow density optimization using a fixed snow density (0.24 g cm^{-3}) and NH-SDN snow density, respectively. (a) Station-based validation of SWE estimates. Scatter points represent modeled and observed SWE, black lines indicate the 1:1 relation, and red dashed lines show linear fits. (b) Spatial comparison of SWE estimates from GlobSnow, NH-SDN-optimized SWE, and station observations.

https://doi.org/10.5194/essd-2026-689
Preprint. Discussion started: 2 November 2026
© Author(s) 2026. CC BY 4.0 License.



5 Discussion

5.1 Advantages of NH-SDN

Although reanalysis products such as ERA5-Land and GLDAS provide continuous snow density datasets over the Northern Hemisphere, snow density in these systems is primarily simulated through snow parameterization schemes within land surface process models, without direct assimilation of in-situ observations (Bian et al., 2019). In addition, process-based models impose physical constraints that can artificially limit snow density variability. For example, the Noah Land Surface Model applies an upper bound of 400 kg m^{-3}, leading to underestimation of extreme snow density values, while the Catchment Land Surface Model (CLSM) initializes snow density at a fixed value of 150 kg m^{-3} and subsequently simulates densification through compaction processes (Toure et al., 2018). Such fixed initial conditions neglect spatial heterogeneity and can result in substantial underestimation of snow density, particularly in mountainous areas.

In contrast to reanalysis products generated by purely physics-based process models, NH-SDN integrates snow state variables derived from reanalysis products with in-situ snow density observations across the Northern Hemisphere. By combining observational constraints with environmental predictors, NH-SDN learns nonlinear relations among observed snow density, process-model outputs, meteorological conditions, snow properties, vegetation characteristics, and topographic factors. This data-driven framework enables the correction of systematic biases inherited from physical models while preserving complete spatial and temporal coverage. As a result, while maintaining complete spatiotemporal coverage over the Northern Hemisphere, NH-SDN reduces the systematic underestimation present in reanalysis products and improves snow density estimation accuracy, particularly in mountainous regions; RMSE decreases from 0.11 g cm^{-3} for GLDAS-Noah and 0.08 g cm^{-3} for ERA5-Land to 0.042 g cm^{-3} for NH-SDN. These results highlight the value of combining the broad coverage of reanalysis data with the observational information provided by in-situ measurements for large-scale snow density estimation.

Previous data-driven approaches are generally developed at regional scales, modeling nonlinear relations between snow density and covariates within limited areas. They are often trained at single time steps and spatial locations, resulting in weak generalization and limited spatiotemporal continuity (Sun et al., 2024b, a). Such relations may not be directly transferable across regions because the dominant controls on snow density vary among snow climates and environmental regimes. In this study, firstly, we integrate in-situ snow density observations across the Northern Hemisphere, covering multiple snow classes and diverse terrain conditions beyond previous regional datasets. Guided by snow formation mechanisms and feature contribution analysis, we carefully select key predictors to effectively characterize snow density variability across different environmental regimes. Secondly, we introduce a spatiotemporal cube as the model input, enabling SDN-Net to jointly exploit spatial neighborhood context and short-term temporal dynamics. In the independent spatial test over Eurasia, SDN-Net achieves an R^2 of 0.646, compared with 0.565 for RF and 0.564 for XGBoost, demonstrating the value of incorporating spatiotemporal context. This improvement indicates that snow density should not be regarded solely as an instantaneous pointwise response to local environmental conditions; rather, its estimation benefits from explicitly accounting for the spatial

https://doi.org/10.5194/essd-2026-689
Preprint. Discussion started: 2 November 2026
© Author(s) 2026. CC BY 4.0 License.



context and recent evolution of the snowpack. Thirdly, we develop a hybrid ViT-CNN architecture to enhance spatiotemporal representation. The ViT component captures long-range spatial dependencies, while CNNs extract local textures and fine-grained spatial details. This complementarity enables SDN-Net to achieve both global contextual modeling and detailed representation in complex terrain. In the independent temporal test, SDN-Net achieves R^2 values of 0.652 in North America and 0.694 in Eurasia, compared with 0.630 and 0.668 for Times-UNet, and 0.585 and 0.636 for Times-ViT, respectively. These results suggest that snow density variability reflects both local and large-scale spatial controls. Moreover, we incorporate a channel attention mechanism to adaptively refine environmental feature representations across snow density evolution stages, providing additional flexibility for representing stage-dependent snow density variations.

5.2 Potential applications and future perspectives

The spatially continuous NH-SDN dataset provides new insights into snow density patterns and long-term regional variations, particularly in areas with limited observational coverage. In montane forests, available observations are mainly concentrated in eastern North America and northern Europe, resulting in uneven spatial representation and potential sampling biases in existing snow density estimates (Zhao et al., 2023). By extending coverage to observation-sparse regions, NH-SDN reveals lower snow density in the western Appalachian Mountains, especially during the increase stage, and a gradual decline in snow density with increasing latitude across central and eastern North America. In the North American Pan-Arctic region, where observations are limited and tundra environments dominate, NH-SDN indicates that more than half of the pixels have exhibited increasing snow density trends in recent decades. This pattern is broadly consistent with SnowPack simulations of SD and SWE variability in the Pan-Arctic region (Liston and Elder, 2006; Liston and Hiemstra, 2011), suggesting that NH-SDN effectively captures physically meaningful large-scale snowpack responses. However, it should be noted that the SnowPack process model mainly considers meteorological forcing factors such as temperature and snowfall, while neglecting vegetation dynamics and wind-driven snow redistribution processes, which may bias its representation toward increasing snow density during the melt period. Similarly, ERA5-Land reanalysis based on CROCUS shows smoothed variability during stable stages and fails to accurately capture decreasing snow density trends in Russia and increasing trends in western North America; it also tends to overestimate certain trends during late winter (February–April) (Li et al., 2026). In contrast, NH-SDN partially reduces these biases in trend estimation, identifying increasing snow density trends during the increase stage in Alaska and the Kamchatka Peninsula, while revealing decreasing trends across western Russia and northern Europe throughout the snow season.

Beyond characterizing snow density itself, higher-accuracy snow density data play a critical role in improving snow water resource estimation and hydrological modeling, particularly in cold-region and mountainous basins where snowmelt dominates the hydrological cycle. Snow density uncertainty remains a primary source of error in SWE estimation. Improved snow density parameterization can enhance SWE retrieval from SD observations. More realistic dynamic representations of snow density can also reduce systematic biases in passive microwave SWE products (Jonas et al., 2009; Li et al., 2025). Since SWE is a key variable linking snow storage to meltwater generation, improved snow density further contributes to a

https://doi.org/10.5194/essd-2026-689
Preprint. Discussion started: 2 November 2026
© Author(s) 2026. CC BY 4.0 License.


more accurate simulation of snowmelt runoff timing and magnitude in snow-dominated basins. Within data assimilation frameworks, incorporating high-quality snow density information into physically based snow models improves the representation of snow microphysical processes, thereby enhancing the joint simulation of SD and SWE (Shrestha and Barros, 2025).

Improved snow density also strengthens the simulation of snow thermal insulation effects. Biases in snow density can propagate into errors in snow thermal conductivity, leading to systematic deviations in simulated ground thermal regimes and permafrost extent (Cao et al., 2020, 2022). Therefore, higher-accuracy snow density datasets can further reduce uncertainties in land surface temperature modeling, improve the representation of soil freeze–thaw dynamics, and ultimately enhance the reliability of permafrost distribution and change assessments under climate warming conditions.

5.3 Uncertainty and limitations

Despite the improvements in accuracy, spatiotemporal continuity, and spatial coverage that NH-SDN offers over existing products, several sources of uncertainty should be acknowledged.

The first source stems from the in-situ observation data itself. Snow density measurements in the training dataset integrate observations collected from multiple countries and agencies, with differences in observation periods, instruments, and methods. For example, the Canadian CanSWE dataset integrates records from federal, provincial, and hydropower networks. Methods include manual snow courses and snow tube sampling, as well as automated snow pillows and snow scales (Vionnet et al., 2021). Manual observations are accurate but temporally sparse, while automated sensors provide continuous measurements but may introduce systematic differences. Secondly, a related concern is the spatial unevenness of the training data, with dense coverage in western North America, Northern Europe, and East Asia, but sparse observations in central North America and in high mountains such as the Himalayas, limiting model performance in these regions. Although transfer learning is employed in this study to mitigate this issue, uncertainties still remain.

A further limitation concerns the model architecture itself. Although SDN-Net effectively captures complex nonlinear relationships between environmental factors and snow density, it remains primarily data-driven and does not explicitly represent the physical evolution of the snowpack or its interactions with hydrological and energy exchange processes. Processes such as snow accumulation, compaction, metamorphism, melt–refreezing, water transport, and heat exchange are therefore not directly embedded in the model. Future work could incorporate these process-based constraints into deep learning frameworks to improve the physical consistency and interpretability of snow density estimates.

Finally, the dataset has a spatial resolution of 0.25°, which is suitable for hemispheric-scale applications such as snow water resource assessment, climate change studies, and hydrological modeling. However, it is still insufficient to resolve fine-scale spatial heterogeneity in mountainous regions, small basins, and complex terrains. As higher-resolution observations and environmental covariates become available, developing snow density products at finer spatial scales, e.g., at 1 km or sub-kilometer resolution, would extend the utility of the NH-SDN framework to basin- and catchment-scale applications.

https://doi.org/10.5194/essd-2026-689
Preprint. Discussion started: 2 November 2026
© Author(s) 2026. CC BY 4.0 License.



6 Code and data availability

The code for SDN-Net is publicly available via the following GitHub repository: https://zenodo.org/records/23795972 (Zhong, 2026). The NH-SDN dataset is stored on Zenodo and can be downloaded here: https://doi.org/10.5281/zenodo.23768969 (Zhang et al., 2026). The dataset contains georeferenced GeoTIFF files organized by year, with each file representing daily snow density estimates across the Northern Hemisphere. Snow density values are provided in units of g cm^{-3}. A mask is applied to exclude snow-free areas. Please refer to the supplementary document included in the repository for more detailed data organization information and file naming conventions.

Companion uncertainty files are provided separately from the primary snow density files. For each valid grid cell and day, these files contain the standard deviation, minimum, and maximum of the five ensemble predictions, all expressed in g cm^{-3}. They use the same grid, spatial reference, daily time coverage, and valid-data mask as the primary product, allowing direct matching by date and grid location. The accompanying documentation specifies the file naming conventions, NoData values, ensemble size, and standard-deviation definition. Details of the uncertainty analysis are provided in Appendix C.

7 Conclusion

This study presents SDN-Net, a spatiotemporal deep learning framework for snow density estimation, and uses it to generate a new snow density dataset for the Northern Hemisphere. The dataset provides accurate and spatially continuous snow density data for long-term applications.

SDN-Net integrates several complementary designs. First, a multi-branch encoder separately processes dynamic environmental variables, including four consecutive time steps of dynamic snow, meteorological, and vegetation variables; static geographic factors; and a temporal vector describing seasonal context. This design captures the diverse environmental controls on snow density variability. Second, the hybrid ViT-CNN architecture combines long-range spatial dependency modeling with local heterogeneity representation, providing spatial context beyond point-based machine learning models (RF and XGBoost) and single-architecture deep learning models (Times-UNet and Times-ViT). Finally, an observation-weighted loss function prioritizes grid cells with more frequent and reliable in-situ observations during training. Together, these designs improve spatial continuity, temporal extrapolation, and regional generalization, resulting in consistently better performance than existing machine learning and single-architecture models.

Using SDN-Net, this study develops NH-SDN, the first observation-constrained daily snow density dataset for the Northern Hemisphere at 0.25° spatial resolution from 1982 to 2025. By integrating observational constraints with the spatiotemporal coverage of reanalysis data, NH-SDN overcomes the sparse distribution of in-situ measurements and corrects systematic biases in existing reanalysis products. Compared with ERA5-Land and GLDAS-Noah, NH-SDN achieves higher accuracy across different months, snow classes, and elevation zones, with RMSE values reduced to 0.042 g cm^{-3} above 2 km and 0.053 g cm^{-3} in maritime regions. NH-SDN also better captures seasonal evolution, spatial variability, and interannual trends. By correcting systematic biases in existing reanalysis products, it reveals previously underestimated spatiotemporal patterns

https://doi.org/10.5194/essd-2026-689
Preprint. Discussion started: 2 November 2026
© Author(s) 2026. CC BY 4.0 License.



of snow density changes in regions including the western Appalachian Mountains, North American Pan-Arctic tundra, western Russia, and northern Europe. Application of NH-SDN to GlobSnow further improves SWE estimation, demonstrating that improved snow density representation can directly enhance the reliability of snow water resource assessment.

Overall, SDN-Net provides a framework for integrating observations, Northern Hemisphere-wide reanalysis data, and multisource environmental information to generate spatially continuous snow density estimates. NH-SDN establishes a reliable, observation-constrained, long-term daily dataset for investigating snow density variability across the Northern Hemisphere and supports snowpack, hydrological, and cryospheric research.

Appendix A. Data partitioning for model development and independent evaluation

Table A1 summarizes the data partition sizes for the spatial and temporal holdout experiments across North America and Eurasia. In the spatial experiment, the three subsets share the same dates and input patch windows but use separate observation-target masks based on station membership, resulting in identical patch counts within each region. In the temporal experiment, the subsets contain different observation dates and therefore differ in both observation-day and patch counts.

Table A1. Data partition sizes for model training, internal validation, and independent testing across North America and Eurasia under the spatial and temporal holdout experiments.

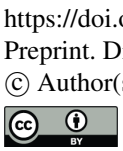
(a) Spatial holdout experiment

Region	Subset	No. of stations	No. of patch samples
North America	Training	8906	19643
	Internal validation	989	
	Independent test	2119	
Eurasia	Training	2340	3535
	Internal validation	260	
	Independent test	428	

(b) Temporal holdout experiment

Region	Subset	No. of days	No. of patch samples
North America	Training	5835	15340
	Internal validation	649	1696
	Independent test	967	2597
Eurasia	Training	1066	2732
	Internal validation	119	299
	Independent test	201	504

https://doi.org/10.5194/essd-2026-689
Preprint. Discussion started: 2 November 2026
© Author(s) 2026. CC BY 4.0 License.



For the spatial holdout experiment, patch counts refer to the shared spatial-temporal input windows. The training, internal-validation, and independent-test subsets use identical input windows but different station-based observation-target masks; therefore, their patch counts should not be summed to obtain the number of unique input patches.

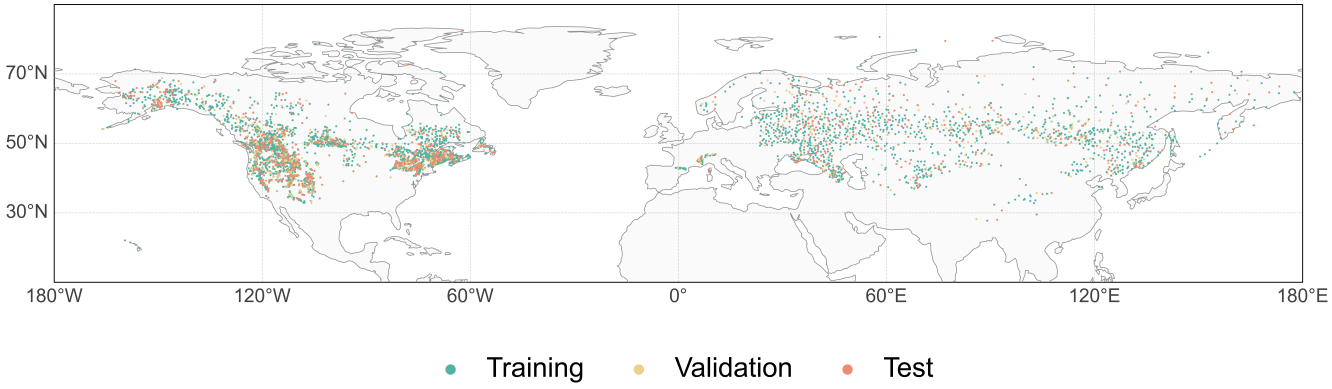


Figure A1. Spatial distribution of in-situ snow density observation sites used for model training, internal validation, and independent spatial testing across the Northern Hemisphere. Green, yellow, and red points indicate observation locations represented in the training, internal-validation, and independent-test subsets, respectively.

Appendix B. Final input variables for the regional SDN-Net models

Following the SHAP-based feature selection described in Section 2.2, the environmental variables appearing among the 14 highest-ranked variables at any snow density evolution stage were combined to form the environmental input set for each region. Spatial, topographic, and temporal variables, together with snow class, were additionally retained as described in Section 3.2.1. Tables B1 and B2 provide the complete final input lists for the North American and Eurasian models.

Table B1. Final input variables for the North American SDN-Net model.

Feature category	Feature
Snow characteristics	Surface albedo, snow albedo, snow cover fraction, snow density distribution, snow depth, 24h cumulative snowfall, snow pressure, snow surface temperature, snow class
Meteorological	2m air temperature, soil surface temperature
Vegetation	High vegetation LAI, low vegetation LAI
Temporal	Day of hydrological year; solar declination, latitude, angular speed
Spatial	Longitude, latitude
Topographic	Elevation, slope, aspect

https://doi.org/10.5194/essd-2026-689
Preprint. Discussion started: 2 November 2026
© Author(s) 2026. CC BY 4.0 License.



Open Access Earth System Science Data Discussions

Table B2. Final input variables for the Eurasian SDN-Net model.

Feature category	Feature
Snow characteristics	Surface albedo, snow albedo, snow cover fraction, snow density distribution, snow depth, 24h cumulative snowfall, snow pressure, snow surface temperature, snow class
Meteorological	2m air temperature, 10m northward wind, 10m eastward wind, soil surface temperature
Vegetation	High vegetation LAI
Temporal	Day of hydrological year; solar declination, latitude, angular speed
Spatial	Longitude, latitude
Topographic	Elevation, slope, aspect

Appendix C. Uncertainty quantification

Ensemble-based uncertainty assessments have been used in recent data products (Ouyang et al., 2026; Zhang et al., 2024). Here, we train five SDN-Net models for each region using five different random seeds, while keeping the training data, input variables, architecture, and hyperparameters unchanged. The seeds control random weight initialization and stochastic training processes, including sample shuffling, producing five sets of learned model weights. All five members follow the same inference, mosaicking, and masking procedures as the primary NH-SDN product. For each valid grid cell and day, we calculate the standard deviation, minimum, and maximum of the five predictions and release these statistics as separate companion files.

Fig. C1 shows that ensemble-based uncertainty is relatively low during the increase, stable, and consolidation stages but higher during the decrease stage. Spatially, higher uncertainty is mainly observed in areas north of 65°N and in the southern Tibetan Plateau. These patterns reflect differences in the sensitivity of snow density predictions to training randomness across stages and regions.

https://doi.org/10.5194/essd-2026-689
Preprint. Discussion started: 2 November 2026
© Author(s) 2026. CC BY 4.0 License.



Open Access Earth System Science Data Discussions

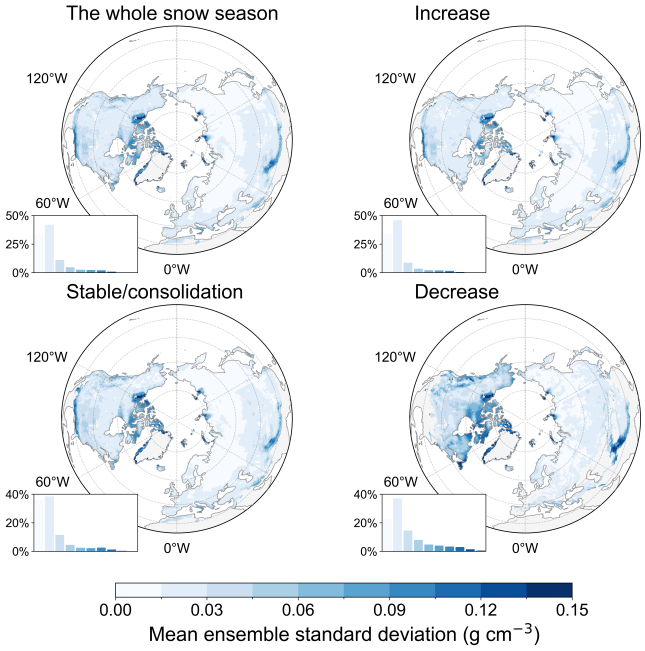


Figure C1. Spatial distribution of the mean daily ensemble standard deviation of NH-SDN during the whole snow season and different snow density evolution stages. Daily standard deviations across the five ensemble members are averaged over valid days at each grid cell. The stable and consolidation stages correspond to Eurasia and North America, respectively. Insets show the percentage distribution of valid grid cells across standard-deviation intervals.

Author contributions

XZ and PX conceptualized and designed the study. LZ, YL, and LS acquired the raw data and performed data processing. LZ developed and implemented the model, performed validation, visualized the results, and wrote the manuscript. LZ and DD explored and refined the model optimization strategies. LZ, XZ, YL, DD, YB, PX, LS, YL, JG, and SZ edited and revised the manuscript.

Competing interests

The authors declare that they have no conflict of interest.

https://doi.org/10.5194/essd-2026-689
Preprint. Discussion started: 2 November 2026
© Author(s) 2026. CC BY 4.0 License.



Open Access Earth System Science Data Discussions

Disclaimer

The authors are solely responsible for the content of this paper, including the use of place names, geographical boundaries, maps, and institutional information. The views and interpretations expressed in this work are those of the authors and do not necessarily represent those of the publisher or affiliated institutions.

Financial support

This work was funded by the National Natural Science Foundation of China (Grant Nos. 42471410 and 42571382) and the AI and AI for Science Project of Nanjing University (Grant No. 020914380141). We are grateful to the High-Performance Computing Center, Nanjing University, for computational support.

References

Barnett, T. P., Adam, J. C., and Lettenmaier, D. P.: Potential impacts of a warming climate on water availability in snow-dominated regions, Nature, 438, 303–309, https://doi.org/10.1038/nature04141, 2005.

Bertasius, G., Wang, H., and Torresani, L.: Is Space-Time Attention All You Need for Video Understanding?, in: Proceedings of the 38th International Conference on Machine Learning (ICML 2021), 833–824, https://doi.org/10.48550/arXiv.2102.05095, 2021.

Bian, Q., Xu, Z., Zhao, L., Zhang, Y.-F., Zheng, H., Shi, C., Zhang, S., Xie, C., and Yang, Z.-L.: Evaluation and Intercomparison of Multiple Snow Water Equivalent Products over the Tibetan Plateau, J. Hydrometeorol., 20, 2043–2055, https://doi.org/10.1175/JHM-D-19-0011.1, 2019.

Bonner, H. M., Raleigh, M. S., and Small, E. E.: Isolating forest process effects on modelled snowpack density and snow water equivalent, Hydrol. Processes, 36, e14475, https://doi.org/10.1002/hyp.14475, 2022.

Bormann, K. J., Westra, S., Evans, J. P., and McCabe, M. F.: Spatial and temporal variability in seasonal snow density, J. Hydrol., 484, 63–73, https://doi.org/10.1016/j.jhydrol.2013.01.032, 2013.

Brown, R. D., Fang, B., and Mudryk, L.: Update of Canadian Historical Snow Survey Data and Analysis of Snow Water Equivalent Trends, 1967–2016, Atmos. Ocean, 57, 149–156, https://doi.org/10.1080/07055900.2019.1598843, 2019.

Broxton, P. D., Van Leeuwen, W. J. D., and Biederman, J. A.: Improving Snow Water Equivalent Maps With Machine Learning of Snow Survey and Lidar Measurements, Water Resour. Res., 55, 3739–3757, https://doi.org/10.1029/2018WR024146, 2019.

Brucker, L., Royer, A., Picard, G., Langlois, A., and Fily, M.: Hourly simulations of the microwave brightness temperature of seasonal snow in Quebec, Canada, using a coupled snow evolution–emission model, Remote Sens. Environ., 115, 1966–1977, https://doi.org/10.1016/j.rse.2011.03.019, 2011.

© Author(s) 2026. CC BY 4.0 License.

Bruland, O., Færevåg, Å., Steinsland, I., Liston, G. E., and Sand, K.: Weather SDM: estimating snow density with high precision using snow depth and local climate, Hydrol. Res., 46, 494–506, https://doi.org/10.2166/nh.2015.059, 2015.

Brun, E., Vionnet, V., Boone, A., Decharme, B., Peings, Y., Valette, R., Karbou, F., and Morin, S.: Simulation of Northern Eurasian Local Snow Depth, Mass, and Density Using a Detailed Snowpack Model and Meteorological Reanalyses, J. Hydrometeorol., 14, 203–219, https://doi.org/10.1175/JHM-D-12-012.1, 2013.

Bulygina, O. N., Groisman, P. Y., Razuvaev, V. N., and Korshunova, N. N.: Changes in snow cover characteristics over Northern Eurasia since 1966, Environ. Res. Lett., 6, 045204, https://doi.org/10.1088/1748-9326/6/4/045204, 2011.

Cao, B., Gruber, S., Zheng, D., and Li, X.: The ERA5-Land soil temperature bias in permafrost regions, Cryosphere, 14, 2581–2595, https://doi.org/10.5194/tc-14-2581-2020, 2020.

Cao, B., Arduini, G., and Zsoter, E.: Brief communication: Improving ERA5-Land soil temperature in permafrost regions using an optimized multi-layer snow scheme, Cryosphere, 16, 2701–2708, https://doi.org/10.5194/tc-16-2701-2022, 2022.

Cao, Y. and Barros, A. P.: Topographic controls on active microwave behavior of mountain snowpacks, Remote Sens. Environ., 284, 113373, https://doi.org/10.1016/j.rse.2022.113373, 2023.

Carabajal, C. C., Harding, D. J., Boy, J.-P., Danielson, J. J., Gesch, D. B., and Suchdeo, V. P.: Evaluation of the Global Multi-Resolution Terrain Elevation Data 2010 (GMTED2010) using ICESat geodetic control, International Symposium on Lidar and Radar Mapping Technologies, 82861Y, https://doi.org/10.1117/12.912776, 2011.

Champollion, N., Picard, G., Arnaud, L., Lefebvre, É., Macelloni, G., Rémy, F., and Fily, M.: Marked decrease in the near-surface snow density retrieved by AMSR-E satellite at Dome C, Antarctica, between 2002 and 2011, Cryosphere, 13, 1215–1232, https://doi.org/10.5194/tc-13-1215-2019, 2019.

Che, T., Dai, L., and Li, X.: Spatiotemporal distribution of seasonal snow density in the Northern Hemisphere based on in situ observation, Res. Cold Arid Reg., 17, 137–144, https://doi.org/10.1016/j.rcar.2025.02.004, 2025.

Clark, M. P., Hendrikx, J., Slater, A. G., Kavetski, D., Anderson, B., Cullen, N. J., Kerr, T., Örn Hreinsson, E., and Woods, R. A.: Representing spatial variability of snow water equivalent in hydrologic and land-surface models: A review, Water Resour. Res., 47, 2011WR010745, https://doi.org/10.1029/2011WR010745, 2011.

Cowherd, M., Mital, U., Rahimi, S., Girotto, M., Schwartz, A., and Feldman, D.: Climate change-resilient snowpack estimation in the Western United States, Commun. Earth Environ., 5, 337, https://doi.org/10.1038/s43247-024-01496-3, 2024.

Dai, L., Che, T., Wang, J., and Zhang, P.: Snow depth and snow water equivalent estimation from AMSR-E data based on a priori snow characteristics in Xinjiang, China, Remote Sens. Environ., 127, 14–29, https://doi.org/10.1016/j.rse.2011.08.029, 2012.

Dawson, N., Broxton, P., Zeng, X., Leuthold, M., Barlage, M., and Holbrook, P.: An Evaluation of Snow Initializations in NCEP Global and Regional Forecasting Models, J. Hydrometeorol., 17, 1885–1901, https://doi.org/10.1175/JHM-D-15-0227.1, 2016.

https://doi.org/10.5194/essd-2026-689
Preprint. Discussion started: 2 November 2026
© Author(s) 2026. CC BY 4.0 License.

Dozier, J. and Shi, J.: Estimation of snow water equivalence using SIR-C/X-SAR. I. Inferring snow density and subsurface properties, IEEE Trans. Geosci. Remote Sens., 38, 2465–2474, https://doi.org/10.1109/36.885195, 2000.

Dutra, E., Balsamo, G., Viterbo, P., Miranda, P. M. A., Beljaars, A., Schär, C., and Elder, K.: An Improved Snow Scheme for the ECMWF Land Surface Model: Description and Offline Validation, J. Hydrometeorol., 11, 899–916, https://doi.org/10.1175/2010JHM1249.1, 2010.

Fassnacht, S. R., Dressler, K. A., and Bales, R. C.: Snow water equivalent interpolation for the Colorado River Basin from snow telemetry (SNOTEL) data, Water Resour. Res., 39, 2002WR001512, https://doi.org/10.1029/2002WR001512, 2003.

Fontrodona-Bach, A., Schaefli, B., Woods, R., Teuling, A. J., and Larsen, J. R.: NH-SWE: Northern Hemisphere Snow Water Equivalent dataset based on in situ snow depth time series, Earth Syst. Sci. Data, 15, 2577–2599, https://doi.org/10.5194/essd-15-2577-2023, 2023.

Gao, S., Li, Z., Zhang, P., Chen, Q., Zeng, J., Zhao, C., Liu, C., and Zheng, Z.: Global Sensitivity Analysis of the MEMLS Model for Retrieving Snow Water Equivalent, IEEE Trans. Geosci. Remote Sens., 60, 1–15, https://doi.org/10.1109/TGRS.2021.3134695, 2022.

Gao, X., Pan, J., Peng, Z., Zhao, T., Bai, Y., Yang, J., Jiang, L., Shi, J., and Husi, L.: Snow Density Retrieval in Quebec Using Space-Borne SMOS Observations, Remote Sens., 15, 2065, https://doi.org/10.3390/rs15082065, 2023.

Gouttevin, I., Menegoz, M., Dominé, F., Krinner, G., Koven, C., Ciais, P., Tarnocai, C., and Boike, J.: How the insulating properties of snow affect soil carbon distribution in the continental pan-Arctic area, J. Geophys. Res.: Biogeosci., 117, 2011JG001916, https://doi.org/10.1029/2011JG001916, 2012.

Hao, J., Mind'je, R., Feng, T., and Li, L.: Performance of snow density measurement systems in snow stratigraphies, Hydrol. Res., 52, 834–846, https://doi.org/10.2166/nh.2021.133, 2021.

Hu, J., Shen, L., Albanie, S., Sun, G., and Wu, E.: Squeeze-and-Excitation Networks, IEEE Trans. Pattern Anal. Mach. Intell., 42, 2011–2023, https://doi.org/10.1109/TPAMI.2019.2913372, 2020.

Huning, L. S. and AghaKouchak, A.: Global snow drought hot spots and characteristics, Proc. Natl. Acad. Sci., 117, 19753–19759, https://doi.org/10.1073/pnas.1915921117, 2020.

Jonas, T., Marty, C., and Magnusson, J.: Estimating the snow water equivalent from snow depth measurements in the Swiss Alps, J. Hydrol., 378, 161–167, https://doi.org/10.1016/j.jhydrol.2009.09.021, 2009.

Kneifel, S., Löhnert, U., Battaglia, A., Crewell, S., and Siebler, D.: Snow scattering signals in ground-based passive microwave radiometer measurements, J. Geophys. Res.: Atmos., 115, 2010JD013856, https://doi.org/10.1029/2010JD013856, 2010.

Kosaka, Y., Kobayashi, S., Harada, Y., Kobayashi, C., Naoe, H., Yoshimoto, K., Harada, M., Goto, N., Chiba, J., Miyaoka, K., Sekiguchi, R., Deushi, M., Kamahori, H., Nakaegawa, T., Tanaka, T. Y., Tokuhiro, T., Sato, Y., Matsushita, Y., and Onogi, K.: The JRA-3Q Reanalysis, J. Meteorol. Soc. Jpn., II, 102, 49–109, https://doi.org/10.2151/jmsj.2024-004, 2024.

Kozlov, M. V.: Snowpack changes around a nickel–copper smelter at Monchegorsk, northwestern Russia, Can. J. For. Res., 31, 1684–1690, https://doi.org/10.1139/cjfr-31-10-1684, 2001.

© Author(s) 2026. CC BY 4.0 License.



Lee, J. H. and Wang, W.: Characterization of snow cover using ground penetrating radar for vehicle trafficability – Experiments and modeling, J. Terramech., 46, 189–202, https://doi.org/10.1016/j.jterra.2009.03.004, 2009.

Leys, C., Klein, O., Dominicy, Y., and Ley, C.: Detecting multivariate outliers: Use a robust variant of the Mahalanobis distance, J. Exp. Soc. Psychol., 74, 150–156, https://doi.org/10.1016/j.jesp.2017.09.011, 2018.

Li, M., Xiao, P., Zhang, X., Feng, X., and Zhu, L.: An improved approach of dry snow density estimation using C-band synthetic aperture radar data, ISPRS J. Photogramm. Remote Sens., 191, 49–67, https://doi.org/10.1016/j.isprsjprs.2022.07.002, 2022.

Li, Y., Miao, X., Hu, X., Wang, L., Zhang, X., Xiao, P., and Guo, W.: Integrated evaluation of snow density reanalysis products in the Northern Hemisphere, J. Hydrol., 669, 135071, https://doi.org/10.1016/j.jhydrol.2026.135071, 2026.

Li, Z., Wu, X., Zhang, W., Zhong, X., Yue, M., Li, Y., Shen, Y., and Chen, R.: High-resolution snow water equivalent estimation derived from downscaled snow depth and non-constant snow density in Chinese Altai Mountains, J. Hydrol., 661, 133708, https://doi.org/10.1016/j.jhydrol.2025.133708, 2025.

Lievens, H., Demuzere, M., Marshall, H.-P., Reichle, R. H., Brucker, L., Brangers, I., De Rosnay, P., Dumont, M., Girotto, M., Immerzeel, W. W., Jonas, T., Kim, E. J., Koch, I., Marty, C., Saloranta, T., Schöber, J., and De Lannoy, G. J. M.: Snow depth variability in the Northern Hemisphere mountains observed from space, Nat. Commun., 10, 4629, https://doi.org/10.1038/s41467-019-12566-y, 2019.

Liston, G. E. and Elder, K.: A Distributed Snow-Evolution Modeling System (SnowModel), J. Hydrometeorol., 7, 1259–1276, https://doi.org/10.1175/JHM548.1, 2006.

Liston, G. E. and Hiemstra, C. A.: The Changing Cryosphere: Pan-Arctic Snow Trends (1979–2009), J. Clim., 24, 5691–5712, https://doi.org/10.1175/JCLI-D-11-00081.1, 2011.

Lundberg, S. and Lee, S.-I.: A Unified Approach to Interpreting Model Predictions, in: Advances in Neural Information Processing Systems (NeurIPS) 2017, https://doi.org/10.48550/arXiv.1705.07874, 2017.

Luojus, K., Pulliainen, J., Takala, M., Lemmetyinen, J., Mortimer, C., Derksen, C., Mudryk, L., Moisander, M., Hiltunen, M., Smolander, T., Ikonen, J., Cohen, J., Salminen, M., Norberg, J., Veijola, K., and Venäläinen, P.: GlobSnow v3.0 Northern Hemisphere snow water equivalent dataset, Sci. Data, 8, 163, https://doi.org/10.1038/s41597-021-00939-2, 2021.

Mavrovic, A., Sonnentag, O., Lemmetyinen, J., Voigt, C., Rutter, N., Mann, P., Sylvain, J.-D., and Roy, A.: Environmental controls of winter soil carbon dioxide fluxes in boreal and tundra environments, Biogeosciences, 20, 5087–5108, https://doi.org/10.5194/bg-20-5087-2023, 2023.

Meehan, T. G., Hojatimalekshah, A., Marshall, H.-P., Deeb, E. J., O'Neel, S., McGrath, D., Webb, R. W., Bonnell, R., Raleigh, M. S., Hiemstra, C., and Elder, K.: Spatially distributed snow depth, bulk density, and snow water equivalent from ground-based and airborne sensor integration at Grand Mesa, Colorado, USA, Cryosphere, 18, 3253–3276, https://doi.org/10.5194/tc-18-3253-2024, 2024.

Meloche, F., Gauthier, F., and Langlois, A.: Snow mechanical property variability at the slope scale – implication for snow mechanical modelling, Cryosphere, 18, 1359–1380, https://doi.org/10.5194/tc-18-1359-2024, 2024.

https://doi.org/10.5194/essd-2026-689
Preprint. Discussion started: 2 November 2026
© Author(s) 2026. CC BY 4.0 License.

Meløysund, V., Leira, B., Høiseth, K. V., and Lisø, K. R.: Predicting snow density using meteorological data, Meteorol. Appl., 14, 413–423, https://doi.org/10.1002/met.40, 2007.

Meromy, L., Molotch, N. P., Link, T. E., Fassnacht, S. R., and Rice, R.: Subgrid variability of snow water equivalent at operational snow stations in the western USA, Hydrol. Processes, 27, 2383–2400, https://doi.org/10.1002/hyp.9355, 2013.

Mizukami, N. and Perica, S.: Spatiotemporal Characteristics of Snowpack Density in the Mountainous Regions of the Western United States, J. Hydrometeorol., 9, 1416–1426, https://doi.org/10.1175/2008JHM981.1, 2008.

Mortimer, C. and Vionnet, V.: Northern Hemisphere in situ snow water equivalent dataset (NorSWE, 1979–2021), Earth Syst. Sci. Data, 17, 3619–3640, https://doi.org/10.5194/essd-2024-602, 2025.

Mulder, V. L., De Bruin, S., and Schaepman, M. E.: Representing major soil variability at regional scale by constrained Latin Hypercube Sampling of remote sensing data, Int. J. Appl. Earth Obs. Geoinf., 21, 301–310, https://doi.org/10.1016/j.jag.2012.07.004, 2013.

Muñoz-Sabater, J., Dutra, E., Agustí-Panareda, A., Albergel, C., Arduini, G., Balsamo, G., Boussetta, S., Choulga, M., Harrigan, S., Hersbach, H., Martens, B., Miralles, D. G., Piles, M., Rodríguez-Fernández, N. J., Zsoter, E., Buontempo, C., and Thépaut, J.-N.: ERA5-Land: a state-of-the-art global reanalysis dataset for land applications, Earth Syst. Sci. Data, 13, 4349–4383, https://doi.org/10.5194/essd-13-4349-2021, 2021.

Ouyang, C., Li, Q., Li, Z., and Wei, S.: An AI-driven reconstruction of global surface temperature with emphasis on refining the Antarctic record, Earth Syst. Sci. Data, 18, 6503–6526, https://doi.org/10.5194/essd-18-6503-2026, 2026.

Pulliainen, J., Luojus, K., Derksen, C., Mudryk, L., Lemmetyinen, J., Salminen, M., Ikonen, J., Takala, M., Cohen, J., Smolander, T., and Norberg, J.: Patterns and trends of Northern Hemisphere snow mass from 1980 to 2018, Nature, 581, 294–298, https://doi.org/10.1038/s41586-020-2258-0, 2020.

Rasmus, S.: Spatial and Temporal Variability of Snow Bulk Density and Seasonal Snow Densification Behavior in Finland, Geophysica, 1–2, 53–74, https://doi.org/http://www.geophysica.fi/pdf/geophysica_2013_49_1-2_053_rasmus.pdf, 2013.

Reeves, J., Chen, J., Wang, X. L., Lund, R., and Lu, Q. Q.: A Review and Comparison of Changepoint Detection Techniques for Climate Data, J. Appl. Meteorol. Climatol., 46, 900–915, https://doi.org/10.1175/JAM2493.1, 2007.

Rodell, M., Houser, P. R., Jambor, U., Gottschalck, J., Mitchell, K., Meng, C.-J., Arsenault, K., Cosgrove, B., Radakovich, J., Bosilovich, M., Entin, J. K., Walker, J. P., Lohmann, D., and Toll, D.: The Global Land Data Assimilation System, Bull. Am. Meteorol. Soc., 85, 381–394, https://doi.org/10.1175/BAMS-85-3-381, 2004.

Roebber, P. J., Bruening, S. L., Schultz, D. M., and Cortinas, J. V.: Improving Snowfall Forecasting by Diagnosing Snow Density, Weather Forecasting, 18, 264–287, https://doi.org/10.1175/1520-0434(2003)018%3C0264:ISFBDS%3E2.0.CO;2, 2003.

Serreze, M. C., Clark, M. P., Armstrong, R. L., McGinnis, D. A., and Pulwarty, R. S.: Characteristics of the western United States snowpack from snowpack telemetry (SNOTEL) data, Water Resour. Res., 35, 2145–2160, https://doi.org/10.1029/1999WR900090, 1999.

https://doi.org/10.5194/essd-2026-689
Preprint. Discussion started: 2 November 2026
© Author(s) 2026. CC BY 4.0 License.

Shrestha, P. and Barros, A. P.: Assimilation of L-band interferometric synthetic aperture radar (InSAR) snow depth retrievals for improved snowpack quantification, Cryosphere, 19, 2895–2911, https://doi.org/10.5194/tc-19-2895-2025, 2025.

Singh, S., Durand, M., Kim, E., and Barros, A. P.: Bayesian physical–statistical retrieval of snow water equivalent and snow depth from X- and Ku-band synthetic aperture radar – demonstration using airborne SnowSAr in SnowEx'17, Cryosphere, 18, 747–773, https://doi.org/10.5194/tc-18-747-2024, 2024.

Sturm, M. and Liston, G. E.: Revisiting the Global Seasonal Snow Classification: An Updated Dataset for Earth System Applications, J. Hydrometeorol., https://doi.org/10.1175/JHM-D-21-0070.1, 2021.

Sturm, M., Taras, B., Liston, G. E., Derksen, C., Jonas, T., and Lea, J.: Estimating Snow Water Equivalent Using Snow Depth Data and Climate Classes, J. Hydrometeorol., 11, 1380–1394, https://doi.org/10.1175/2010JHM1202.1, 2010.

Sun, L., Zhang, X., Wang, H., Xiao, P., and Wang, Y.: Estimating Daily Snow Density Through a Spatiotemporal Random Forest Model, Water Resour. Res., 60, e2023WR036942, https://doi.org/10.1029/2023WR036942, 2024a.

Sun, L., Zhang, X., Xiao, P., Wang, H., Wang, Y., and Zheng, Z.: Fusing daily snow water equivalent from 1980 to 2020 in China using a spatiotemporal XGBoost model, J. Hydrol., 632, 130876, https://doi.org/10.1016/j.jhydrol.2024.130876, 2024b.

Taylor, K. E.: Summarizing multiple aspects of model performance in a single diagram, J. Geophys. Res.: Atmos., 106, 7183–7192, https://doi.org/10.1029/2000JD900719, 2001.

Toure, A. M., Reichle, R. H., Forman, B. A., Getirana, A., and De Lannoy, G. J. M.: Assimilation of MODIS Snow Cover Fraction Observations into the NASA Catchment Land Surface Model, Remote Sens., 10, 316, https://doi.org/10.3390/rs10020316, 2018.

Valt, M., Guyennon, N., Salerno, F., Petrangeli, A. B., Salvatori, R., Cianfarra, P., and Romano, E.: Predicting new snow density in the Italian Alps: A variability analysis based on 10 years of measurements, Hydrol. Processes, 32, 3174–3187, https://doi.org/10.1002/hyp.13249, 2018.

Venäläinen, P., Luojus, K., Lemmetyinen, J., Pulliainen, J., Moisander, M., and Takala, M.: Impact of dynamic snow density on GlobSnow snow water equivalent retrieval accuracy, Cryosphere, 15, 2969–2981, https://doi.org/10.5194/tc-15-2969-2021, 2021.

Venäläinen, P., Luojus, K., Mortimer, C., Lemmetyinen, J., Pulliainen, J., Takala, M., Moisander, M., and Zschenderlein, L.: Implementing spatially and temporally varying snow densities into the GlobSnow snow water equivalent retrieval, Cryosphere, 17, 719–736, https://doi.org/10.5194/tc-17-719-2023, 2023.

Vionnet, V., Mortimer, C., Brady, M., Arnal, L., and Brown, R.: Canadian historical Snow Water Equivalent dataset (CanSWE, 1928–2020), Earth Syst. Sci. Data, 13, 4603–4619, https://doi.org/10.5194/essd-13-4603-2021, 2021.

Wang, H., Zhang, X., Xiao, P., Che, T., Zheng, Z., Dai, L., and Luan, W.: Towards large-scale daily snow density mapping with spatiotemporally aware model and multi-source data, Cryosphere, 17, 33–50, https://doi.org/10.5194/tc-17-33-2023, 2023.

© Author(s) 2026. CC BY 4.0 License.



Wetlaufer, K., Hendrikx, J., and Marshall, L.: Spatial Heterogeneity of Snow Density and Its Influence on Snow Water Equivalence Estimates in a Large Mountainous Basin, Hydrology, 3, 3, https://doi.org/10.3390/hydrology3010003, 2016.

Winstral, A. and Marks, D.: Long-term snow distribution observations in a mountain catchment: Assessing variability, time stability, and the representativeness of an index site: LONG-TERM SNOW DISTRIBUTION OBSERVATIONS, Water Resour. Res., 50, 293–305, https://doi.org/10.1002/2012WR013038, 2014.

Yan, S., Chen, Y., Hou, Y., Liu, K., Li, X., Xing, Y., Wu, D., Cui, J., Zhou, Y., Pu, W., and Wang, X.: Which global reanalysis dataset has better representativeness in snow cover on the Tibetan Plateau?, Cryosphere, 18, 4089–4109, https://doi.org/10.5194/tc-18-4089-2024, 2024.

Yang, J. W., Jiang, L. M., Lemmetyinen, J., Luojus, K., Takala, M., Wu, S. L., and Pan, J. M.: Validation of remotely sensed estimates of snow water equivalent using multiple reference datasets from the middle and high latitudes of China, J. Hydrol., 590, 125499, https://doi.org/10.1016/j.jhydrol.2020.125499, 2020.

Zhang, X., Zhong, L., and Xiao, P.: NH-SDN: A Deep Learning-Derived Daily 0.25° Snow Density Dataset for the Northern Hemisphere (1982–2025), Zenodo [data set], https://doi.org/10.5281/zenodo.23768969, 2026.

Zhang, Y., Shen, F., Li, R., Li, M., Li, Z., Chen, S., and Sun, X.: AIGD-PFT: the first AI-driven global daily gap-free 4 km phytoplankton functional type data product from 1998 to 2023, Earth Syst. Sci. Data, 16, 4793–4816, https://doi.org/10.5194/essd-16-4793-2024, 2024.

Zhao, W., Mu, C., Han, L., Sun, W., Sun, Y., and Zhang, T.: Spatial and temporal variability in snow density across the Northern Hemisphere, CATENA, 232, 107445, https://doi.org/10.1016/j.catena.2023.107445, 2023.

Zhong, L.: SDN-Net v1.0.0: A Spatiotemporal Framework for Snow Density Estimation, Zenodo [code], https://doi.org/10.5281/zenodo.23795972, 2026.

Zhong, X., Zhang, T., Kang, S., and Wang, J.: Spatiotemporal variability of snow cover timing and duration over the Eurasian continent during 1966–2012, Sci. Total Environ., 750, 141670, https://doi.org/10.1016/j.scitotenv.2020.141670, 2021.